Garcia, Oscar. (2019). System and Algorithm Development to Estimate Oil Thickness and Emulsification. (Bureau of Safety and Environmental Enforcement Oil Spill Response Research Project # E17PC00021).

Report to Bureau of Safety and Environmental Enforcement (BSEE):

System and Algorithm Development to Estimate Oil Thickness and Emulsification

Submitted by:
Oscar Garcia, Chuanmin Hu, Shaojie Sun,
Diana Garcia

Submitted to:
Bureau of Safety and Environmental Enforcement
Oil Spill Response Research Branch

March 29, 2019

EXECUTIVE SUMMARY

Water Mapping, LLC (WM) was awarded to support the Bureau of Safety and Environmental Enforcement's (BSEE) interest in TOPIC 2 of the BAA announcement E17PS00040: "Development of Algorithm and/or Imagery Processing Technology to Measure Emulsion Levels and/or Thickness of Oil Using Various Remote Sensing Tools ". The funded project titled: 'System and Algorithm Development to Estimate Oil Thickness and Emulsification Through a Multisensor Platform' is focus on the implementation of an array of sensors called multispectral imager that would collect data from floating layers of oil and emulsions and that it would be used to derive thickness information from the floating oil. The objective was to build a suite of sensors and configure them to create a real and near-real time system that could be used for oil spill response and assessment operations. This system was successfully developed, calibrated, and tested in different sets of conditions by mounting it on an Unmanned Aerial System (UAS). This technical report includes the scientific basis on which this project was focused and the experiments that we carried out to make this system an operational tool.

This project started with the selection of commercial imagers (multispectral cameras) that fit our needs in terms of wavelengths, resolution, costs, and configurations. Then the project included two phases: Phase 1: Lab Testing, consisted on the elaboration of layers of oil in a controlled setting where we could validate the multispectral imager response to identify different levels of thicknesses, and Phase 2: Field testing, which consisted on the testing on a real life spill scenario where we could demonstrate the potential of the multispectral sensor package.

Our vision is to facilitate this development of an oil spill response system in which remotely sensed images by a UAS are interpreted with validated algorithms providing intelligent classifications of oil thicknesses. This now operational system will help to direct fleet

vessels to locations where responders will have the highest remediation value. Additionally, this system will help to evaluate the magnitude of an oil spill by using oil thickness classification on the quantification of the oil volume discharged.
In this report we present how WM achieved our ultimate goal which is to deliver an image processing algorithm that can be used to process data collected from aerial platforms operating a combination of multispectral and thermal sensors. This algorithm/sensor system demonstrated its capacity of identifying areas and locations of actionable oils to response units. The information generated from the system allowed improved oil mitigation and control actions by responder vessels and for the assessment of the impact and magnitude of the oil spill.

This report is organized so we describe first the Phase 1 which consisted on lab tests at the University of South Florida and two experiments at Ohmsett during the summer of 2018; then we present the results achieved during the Phase 2 which consisted on data collection and processing during the Lake Washington Wellhead oil spill in Louisiana.

System and Algorithm Development to Estimate Oil Thickness and Emulsification

03/2019

Authors:
Oscar Garcia
Water Mapping, LLC

Chuanmin Hu
University of South Florida

Shaojie Sun
University of South Florida

Diana Garcia
Water Mapping, LLC

Prepared under BSEE Contract Number E17PC00021
By
Water Mapping LLC
1041 Edgewater ln
Gulf Breeze, FL 32563

DISCLAIMER

Study concept, oversight, and funding were provided by the US Department of the Interior (DOI), Bureau of Safety and Environmental Enforcement (BSEE), Oil Spill Preparedness Division (OSPD), Response Research Branch (RRB), Sterling, VA, under Contract Number E17PC00021. This report has been reviewed by BSEE, and it has been approved for publication.

The findings and opinions expressed in this report are solely those of the authors and do not necessarily reflect the views and policies of the Bureau of Safety and Environmental Enforcement (BSEE), nor does mention of the trade names or commercial products constitute endorsement or recommendation for use.

ACKNOWLEDGMENTS

Water Mapping would like to thank the invaluable support from BSEE on the development of this work, as well as the collaboration from our colleagues from USF, NOAA, EPA, and the USCG.

Table of Contents

List of Figures

List of Tables

List of Abbreviations and Acronyms

In this section list alphabetically respective abbreviations and acronyms utilized in the report. Below are some example abbreviations.

AVIRIS	The airborne visible/infrared imaging spectrometer
BSEE	Bureau of Safety and Environmental Enforcement
CDOM	Colored dissolved organic matter
CSE	Council of Science Editors
DOI	US Department of the Interior
FOV	Field of View
GPS	Global Positioning System
IR	Infrared
MODIS	Moderate Resolution Imaging Spectroradiometer
NESDIS	National Environmental Satellite, Data, and Information Se
NIR	Near-Infrared Reflectance
NOAA	National Oceanic and Atmospheric Administration
NTUs	Nephelometric Turbidity Units
OSPD	Oil Spill Preparedness Division
RGB	Read, Green, and Blue
RRB	Response Research Branch
SWIR	Short-wave infrared
UAS	Unmanned Aircraft Systems
USF	University of South Florida
USGS	United States Geological Survey
VIS	Visual
WM	Water Mapping
WM-OTS	Water Mapping Oil Thickness Sampler

Phase I: Lab Testing

Optical measurements and interpretation of oil on water

1. Introduction: Scientific Background

Despite the numerous published papers on optical measurements and interpretation of spilled oil on the ocean surface, several significant technical challenges still exist. These challenges make remote estimation of oil slick thickness (or volume) difficult. The experiments and data analyses in this study are meant to address some of these challenges.

1.1 Oil heterogeneity

Oil is highly heterogeneous on the ocean surface. Therefore, a coarse-resolution remote sensing image pixel, such as from MODIS measurements (250-m spatial resolution), may contain surface oil of non-uniform thickness mixed with water (Sun et al., 2016). According to statistics from high-spatial resolution (~ 8 m) AVIRIS measurements, most of the MODIS pixels that contain oil have only a few percent of the pixel covered by thick oil (Sun et al., 2016). The heterogeneity of oil can be easily seen from the tank experiment at University of South Florida (Figure 1; tank size is 1.3x0.9x0.5 m by length x width x depth). Oil emulsions tend to spread very slowly in calm conditions because of the high viscosity of oil emulsions. In this experiment, the oil emulsion forms very small patches ranging between a few millimeters to a few centimeters in size.

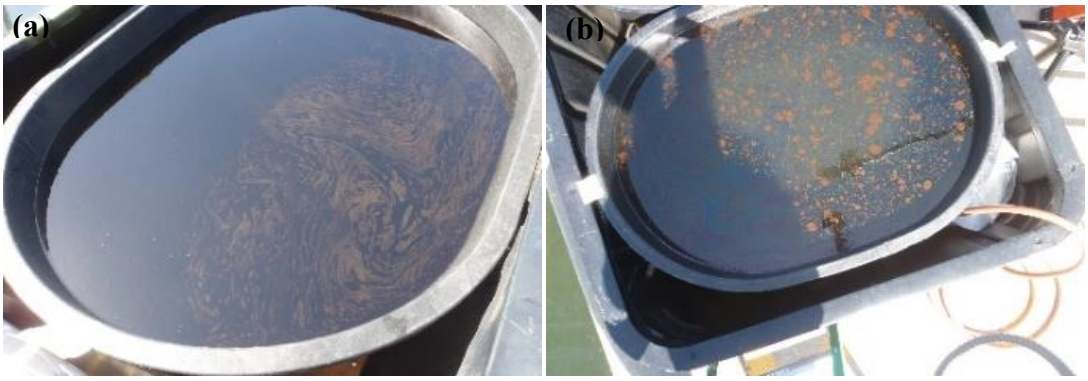

Figure 1. Tank experiment.
Oil distribution is highly heterogeneous on the water surface in the tank experiment. a) crude oil; b) oil emulsion. Both tanks are 1.3x0.9x0.5 m by length x width x depth.

Oil reflectance has a non-linear response to oil thickness (Wettle et al., 2009; Clark et al., 2010). Therefore, the heterogeneity of oil not only makes it difficult to estimate oil thickness from remote sensing imagery, but also makes it difficult to interpret field-measured reflectance because the field of view of a spectroradiometer is often 8-12o with a footprint size of 14 – 21 cm if the spectroradiometer is 1 m away from the water. Even at this size, the oil is still heterogenous within the FOV. This is why to date most oil reflectance experiments have been conducted in the lab with very small sample size (e.g., Clark et al., 2010; Lu et al., 2016). Clearly, new experiments are required to address the heterogeneity issue.

1.2 Difficulty in oil thickness measurements

Nearly all oil experiments do not measurement thickness but estimate thickness from a known volume divided by surface area (e.g., Svejkovsky and Muskat, 2006). Because of the oil heterogeneity, such estimated thickness is the mean thickness while individual spots within the surface area may have different thickness. The lack of field-measured thickness is due to the difficulty in accurate measurements of the thin oil film or layer. Earlier attempts inserted a piece of glass across the water surface and assumed that the oil left on the glass had the same thickness as on the water surface (Svejkovsky and Muskat, 2006). This assumption may lead to large errors. New methods need to be developed to measure surface oil thickness in the field.

1.3 Contrasting results from the literature

The optical response of oil-on-water has been measured several times in the past (e.g., Byfield, 1998; Wettle et al., 2009; Clark et al., 2010). yet results vary substantially (Figure 2). For example, crude oil has strong absorption in the short wavelengths, where the absorption decays exponentially towards longer wavelengths (Byfield, 1998). When oil is emulsified, its mixing with water creates oil–water particles that have strong scattering in all wavelengths. This effect is manifested in the red-Near Infrared (NIR)-ShortWave InfraRed (SWIR) wavelengths (Clark et al., 2010) because of water molecules' negligible scattering in these wavelengths.

Wettle et al. (2009) showed dramatic reflectance changes in blue–green wavelengths but no change in the NIR for different oil thicknesses. In contrast, Clark et al. (2010) showed the opposite. Other field experiments also showed variable results (Figure 2). Given these variable results, it is important to understand what caused the difference.

1.4 Lack of algorithms to classify oil type (crude oil versus oil emulsion) and estimate oil thickness

Despite the many attempts in the past to determine reflectance response to oil-on-water (e.g., Otremba and Piskozub, 2001 & 2003; Otremba et al., 2013), in practice it has been very difficult to develop inversion algorithms to classify oil type (e.g., crude oil versus oil emulsion) and quantify thickness from the oil's reflectance spectra. Many experiments have been attempted for such inversions, mostly under controlled laboratory environments, yet the results often differ for many reasons. In addition to the heterogeneity induced mixed pixel effect, when applied to remote sensing imagery, the results from laboratory-based measurements are always confounded variable solar/viewing conditions, winds, and different water properties from those in the laboratory experiments.

2. Objectives

Given the challenges listed above, the ultimate goal of this study is to develop practical inversion algorithms to be applied to remote sensing imagery for fast response during a spill. Specifically, the objectives are to develop/Implement of a UAS system (platform + sensors) and to develop algorithms for image processing and oil classification/quantification. This will involve the following sub-tasks: 1) Literature review to optimize selection of instrumentation; 2) UAS multisensory array implementation, 3) controlled field experiments (oil tank and Ohmsett facility), and 4) algorithm development.

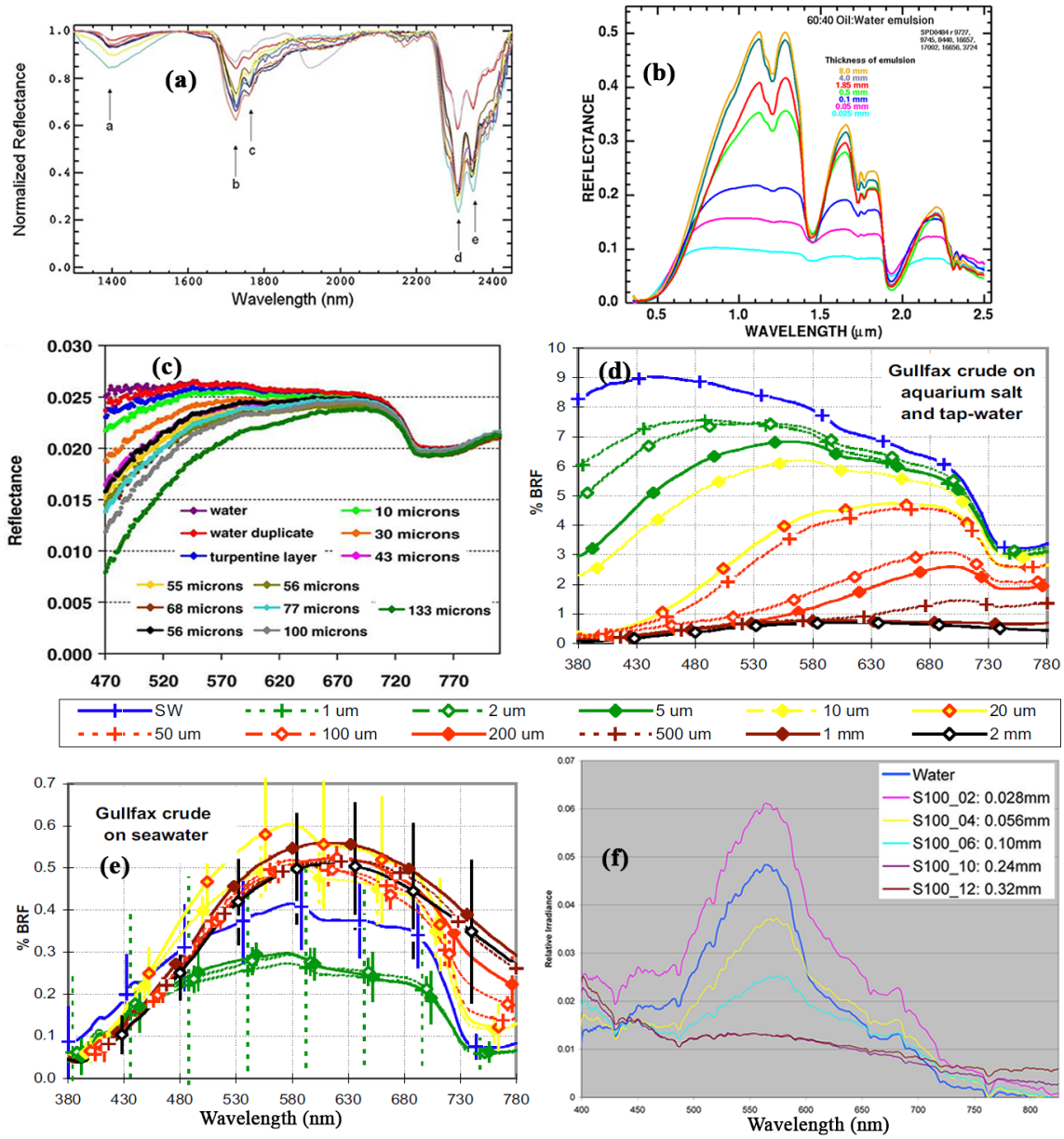

Figure 2. Reflectance of oil and emulsions.
Contrasting reflectance spectra of oil on water measured under different conditions by several groups: a) pure oil: continuum removed reflectance spectra of 17 pure oil samples obtained from the main Brazilian sedimentary basins show features of <a> O–H absorption at 1400nm, C–H absorption features at <b>1720-1730nm, <c>1750-1760nm, <d>2310nm and <e>2350nm (Lammoglia and Filho, 2011). b) oil on water spectra: varying thicknesses of 60:40 oil–water mixing ratio emulsions over quartz plates on an empty painted black glass jar. The emulsions were collected from the Gulf of Mexico (GoM) during the DWH oil spill (Clark et al., 2010). c) oil on water spectra: Gippsland crude oil of different thicknesses on top of pure water, measured in a beaker (Wettle et al., 2009). d) oil on water spectra: Gullfax crude oil of different thicknesses on artificial seawater (Byfield, 1998); (e) oil on water spectra: the same Gullfax crude oil of different thicknesses on dockside seawater (Byfield, 1998). (f) oil on water spectra: Arabian Medium Crude oil of different thicknesses over the background of seawater in Oceanside Harbor, California (Svejkovsky and Muskat, 2006).

3. Methods

3.1 Literature review on oil-water spectral and spatial contrasts

Numerous experiments have been conducted to determine the oil's reflectance spectra using different oil types and experimental settings. Here, we select some representative experiments to compare the results. Of these, reflectance spectra of pure oil (Figure 2a) were obtained from Lammoglia and Filho (2011) and reflectance spectra of oil-on-water (Figures 2b-2e) were obtained from Clark et al. (2010), Wettle et al. (2009), and Byfield (1998), respectively. These spectra were collected from laboratory measurements using artificial light sources and small oil sample size. For comparison, reflectance spectra collected from outdoor harbor water under solar illumination (Figure 2f) were obtained from Svejkovsky and Muskat (2006).

The purpose of this literature review is two folds. First, it will determine whether some rules can be generalized to classify oil types and quantify oil thickness. Second, it will help define the optimal wavelengths for oil spill assessment if a hyperspectral sensor is not feasible.

3.2. Instrumentation design and implementation

Through the literature review, the optimal wavelengths for oil spill assessment are determined. Then, the type of spectrometer suitable for field measurements is determined. Finally, the sensors to be mounted on the UAS are determined.

The literature review indicated the following.

1) Emulsified oil can be differentiated from crude oil from its NIR reflectance (735 - 790nm): high scattering of emulsion enables high spectral reflectance while non-emulsified oil has very low reflectance in the NIR wavelengths (Figure 2). Increasing crude oil thickness would result in a decrease in reflectance in the blue-green wavelengths, which also depend on ambient water properties—blue water or tap water were observed to show a decrease of reflectance in mostly blue wavelengths with increasing oil thickness (Wettle et al., 2009) while a decrease of reflectance in green wavelengths was observed in coastal waters because of CDOM absorption in the blue wavelength and chlorophyll absorption in blue and red wavelengths (Lu et al., 2013; Svejkovsky and Muskat, 2006). Therefore, if a hyperspectral sensor is not possible, at least the following wavelengths should be available for a multi-band sensor: blue, green, red, NIR, and SWIR. Furthermore, to differentiate brown algae from oil emulsion, a band around 620 nm, corresponding to chlorophyll-a absorption maximum, is required (Hu et al., 2015).

2) The apparent temperature of oil detected from a remote platform also increases with oil thickness up to the 2 mm (Svejkovsky et al. 2012). Although the thermal signal may change during the course of a day (Lu et al., 2016), in principle thermal remote sensing can be used to quantify relatively thick oil slicks.
3) Therefore, a combination of thermal remote sensing and multispectral optical RS can be used to differentiate oil slick type and quantify oil slick thickness through calibration and validation using in situ measurements concurrent and collocated with the remote sensing measurements. Briefly, the first step is to detect oil slicks (yes/no) using a spatial contrast in the VIS/NIR imagery. Then, the NIR contrast between oil and water may be used to differentiate whether the oil is emulsified or not. For non-emulsified oil, VIS and thermal IR signals may be used to estimate oil thickness. For emulsified oil, NIR and thermal IR signals may be used to estimate oil thickness.

Based on these observations and considerations, the following sensors were purchased and implemented.

1) A hyperspectral, hand-held, portable spectroradiometer made by Spectral Evolution, Inc., namely the SR-1900 spectroradiometer (Figure 3a). The instrument has 8° field of view and covers a spectral range of 280—1900 nm with a spectral resolution of ≤4 nm in 280—1000 nm and ≤10 nm in 1000—1900 nm. Such a spectral range and resolution are sufficient to measure reflectance of oil-on-water and characterize the spectral shapes and magnitudes.
2) Among a list of commercially available multi-band cameras (e.g., Bayspec, Mapir, Micasense, Sentera, Slantrange, Tetracam), two multiband imaging cameras (Figure 3b) were selected after careful consideration of their spectral bands, signal-to-noise ratios, costs, weights, and easiness of use. These include a MicaSense RedEdge-M™ Multispectral Camera and a Mapir kernel camera. The Micasense camera has five spectral bands: blue (475 nm), green (560 nm), red (668 nm), red edge (717 nm), and NIR1 (840 nm). The Mapir kernel camera has two spectral bands: NIR2 (880 nm) and NIR3 (940 nm), which extend the NIR range of the Micasense camera. Unfortunately, no commercial sensor was available to cover the SWIR wavelengths while meeting the requirements of the above constraints.
3) Calibrated Radiometric Thermal Sensor (Flir Vue Pro R).

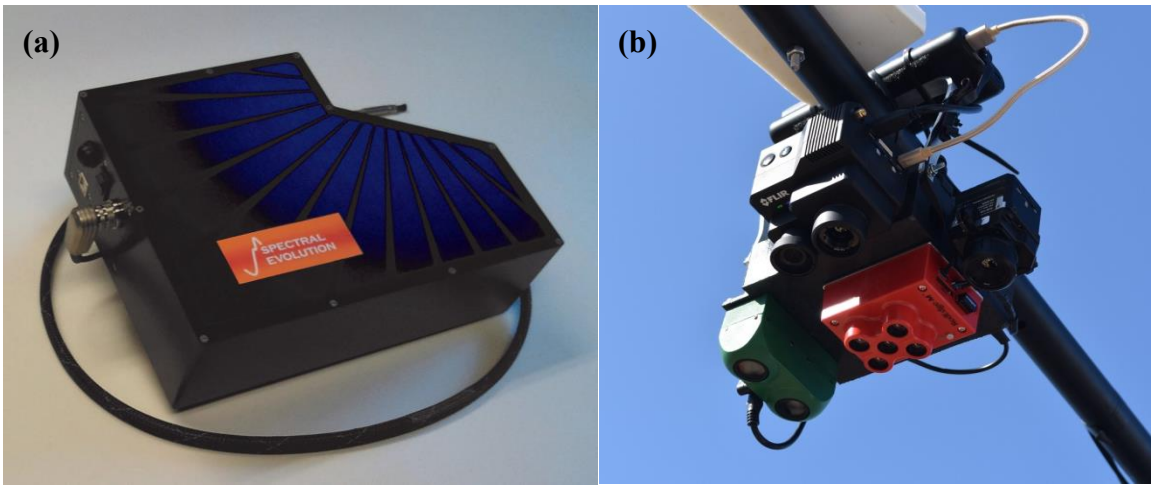

Figure 3 Multispectral sensors.
a) SR-1900 portable spectroradiometer (280 – 1900 nm); b) imaging multiband cameras from Micasense (red one, in bands of 475 nm, 560 nm, 668 nm, 717 nm, and 840 nm) and Mapir (green one, in bands of 880 nm and 940 nm), and thermal cameras.

These instruments were used in the following experiments to measure oil-on-water in order to develop algorithm to interpret the spectral characteristics of oil-on-water and to develop algorithms to classify oil types and estimate oil thickness.

3.3 Two experiments

Two experiments were designed, including the USF oil tank experiment, and the Ohmsett tank experiment.

3.3.1. USF oil tank experiment

The experiment was conducted in March 2018 in the Bayboro Harbor by the seawall at University of South Florida St. Petersburg. In this experiment, known volumes of crude and emulsified oil were put on the water surface in two identical black plastic oval tanks, each with a size of 1.3-m in length, 0.9-m in width, and 0.5-m in depth. The water was pumped from Tampa Bay by the seawall when water temperature was around 28oC. Although chlorophyll content and turbidity were note measured, for this time of year Tampa Bay waters typically have chlorophyll concentrations of a few milligrams per cubic meter and turbidity of a few NTUs. The experimental setup is shown in Figure 4.

Initially, oil on the surface spread fast, but not evenly in the tank even after a few minutes (Figure 4b). Mean surface oil thickness was therefore estimated as the oil volume divided by

surface area of the tank. This thickness represents the equivalent thickness if oil would be evenly distributed in the tank. Three types of oil (HOOPS, ANS and IFO-120) were tested. Each was tested for both crude oil and oil emulsions with various oil thicknesses in Table 1.

For each oil-on-water setting, reflectance was measured with the SR-1900 about 1 m above the tank surface (Figure 4a). At this height, the 8o FOV gave a footprint size of about 14 cm in diameter, which covered multiple oil patches. The resulting reflectance spectra were averaged over three separate measurements, with each measurement an average of ten continuous scans. For each oil-on-water setting, images were also taken by the two imaging cameras and the thermal camera mounted on a fixed platform, with the cameras about 2 m above the tank surface (Figure 4a).

The oils were put on the water surface incrementally from the minimum thickness to the maximum thickness. After measurements of the maximum oil-on-water, oil was collected using strong absorption pads many times until no oil film could be visualized. Then, the remaining water was carefully filtered through using a bio-filter and safely disposed.

Figure 4. USF tank test setup.
a) Oil tank experiment set up in USF St. Petersburg campus by the Bayboro seawall. Two multi-band cameras and a thermal camera are mounted on a tripod frame to collect images from the oil-on-water in the two tanks. The figure also shows Shaojie Sun (on the ladder) and Chuanmin Hu (on the ground) taking reflectance measurements using the SR-1900 spectroradiometer (photo credit: George Graettinger). (b) and (c) Two identical tanks (1.3 x 0.9 x 0.5 m in length x width x depth) filled with Tampa Bay water, where the same volume of b) crude oil and c) emulsified oil are put on the water surface using precise syringes.

Table 1 Sensor wavelengths. The various equivalent thickness of crude oil and oil emulsions used in the USF oil tank experiment (Figure 4), where their images were collected by the multiband and thermal cameras.

	RGB	**475 nm**	**560 nm**	**669 nm**	**717 nm**	**840 nm**	**880 nm**	**940 nm**	**Thermal 2-7um**	**Emissivity**
No oil	✓	✓	✓	✓	✓	✓	✓	✓	✓	✓
0.3µm	✓	✓	✓	✓	✓	✓	✓	✓	✓	✓
1µm	✓	✓	✓	✓	✓	✓	✓	✓	✓	✓
5µm	✓	✓	✓	✓	✓	✓	✓	✓	✓	✓
10µm	✓	✓	✓	✓	✓	✓	✓	✓	✓	✓
50µm	✓	✓	✓	✓	✓	✓	✓	✓	✓	✓
100µm	✓	✓	✓	✓	✓	✓	✓	✓	✓	✓
500µm	✓	✓	✓	✓	✓	✓	✓	✓	✓	✓
>500 µm	✓	✓	✓	✓	✓	✓	✓	✓	✓	✓

The USF oil tank experiment was followed immediately by a beach calibration experiment, with the purpose of calibrating the multi-band camera signals into meaningful reflectance values. The calibration experiment was also used to test the ability of the cameras' sensitivity to differentiate dark objects. The experiment location was chosen at Clam Bayou Park because various ground targets can be found in this location, including grass, high-reflective beach, and more importantly submerged seagrass. The latter has very low reflectance and resamples the low reflectance of crude oil in the marine environment. The setup of the beach experiment is shown in Figure 5. In this experiment, six Lambertian panels with reflectance ranging between 7% and 90% were placed on the ground, which were measured by the SR-1900 spectroradiometer and the multi-band cameras mounted on the UAS (done). Because the former provides well-calibrated surface reflectance, the later signals can be calibrated into reflectance accordingly. The calibration coefficients were then used to convert the images collected in the USF oil tank experiment to multi-band reflectance images.

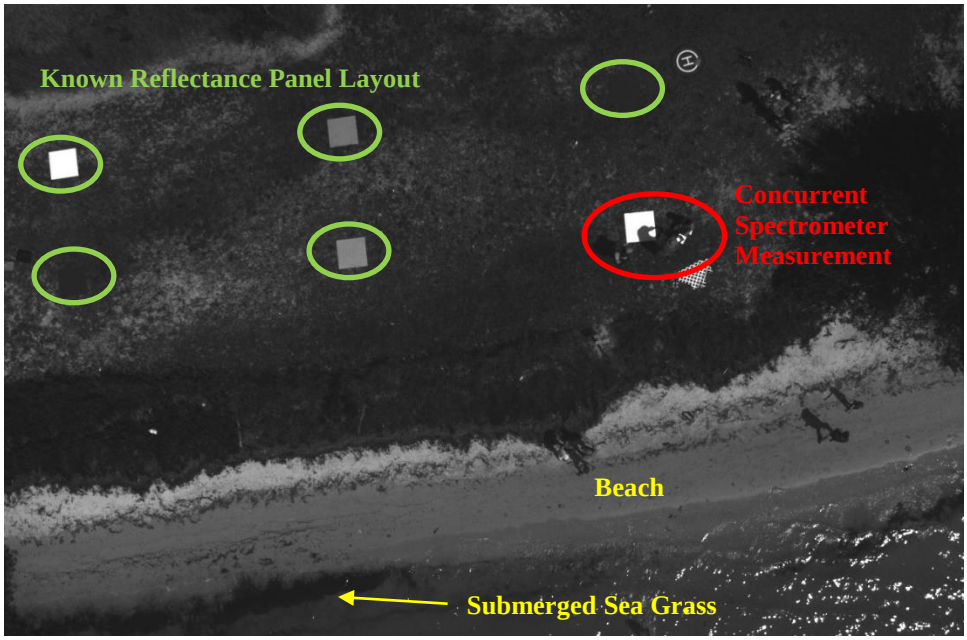

Figure 5. Calibration experiment on the Clay Bayou Park beach, Gulfport, Florida, in March 2018. Six Lambertian panels with known reflectance varying from 7% to 90% are placed on land. These panels were measured by the well-calibrated SR-1900 spectroradiometer and by the un-calibrated multi-band cameras mounted on the UAS (drone), so the latter signals can be calibrated by the former. Red circled area shows Shaojie Sun measuring the radiance of the white panel using the SR-1900 spectroradiometer.

3.3.2. Ohmsett field experiment

The field experiment was conducted at the National Oil Spill Response Research & Renewable Energy Test Facility (Ohmsett) in June 2018. Ohmsett features an above-ground concrete test tank of 203 m long by 20 m wide by 3.4 m deep. The tank was filled with 2.6 million gallons of clear saltwater. The Ohmsett experiment was set up as follows:

1) Black Tarp Setup

Different from previous Ohmsett experiments, a black tarp (Figure 6a, black rectangular target of 20’x30’under the squares) was set up at the bottom of the Ohmsett tank to mimic water reflectance in the natural marine environment. Because the Ohmsett tank is shallow (2.4 meters deep) and the water is clear, sun light in the visible wavelengths can easily penetrate to the bottom of the tank and then get reflected back through the water column, captured by the hand-held SR-1900 spectroradiometer and multi-band cameras. The high reflectance of the tank bottom thus leads to very high reflectance, representing an unrealistic background as compared with the real marine environments. Using the SR-1900 spectroradiometer, we measured a

reflectance of ~25% of the tank water (Figure 6b) in the green wavelengths, which is more than 10 times higher than typical reflectance of coastal waters (i.e., Tampa Bay water, ~2%) and open-ocean water in the Gulf of Mexico (<1%) in the corresponding wavelengths. By introducing a black tarp featuring < ~6% reflectance in the visible wavelengths, the water background becomes much darker, with a surface reflectance much closer to reflectance in typical coastal and open-ocean environments (Figure 6b). All oil square measurements when then conducted on top of the tarp location.

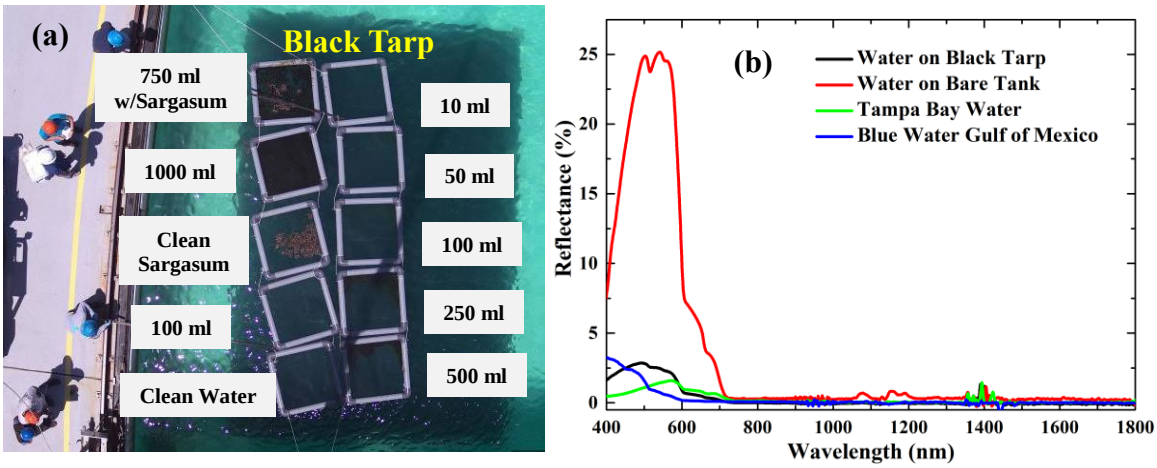

Figure 6. Ohmsett setup.
a) A 20'x30' black tarp was set at the bottom of the Ohmsett tank. All the oil square measurements were then taken on top of the tarp. This setup shows 10 squares featuring HOOPS crude oil of different volumes, oiled and clean Sargassum, and clean water. The marked 1000 ml volume, for example, denotes the total volume of HOOPS oil in the square. If spread evenly, this volume of oil would create a 1000-µm thickness layer in the square. b) Reflectance spectra of Ohmsett tank water on the bare bottom and on the black tarp, compared with reflectance spectra of typical coastal waters from Tampa Bay and typical open-ocean blue waters from the Gulf of Mexico. Without the tarp, Ohmsett water is much brighter (i.e., elevated reflectance between 400 – 700 nm) than most of the natural waters.

2) Oil Square Setup

Squares of 1m x 1m containing crude oil, emulsified oil, Sargassum, and clean water were set on top of the tarp. Sargassum samples were collected from a recent Gulf of Mexico field trip and shipped to the Ohmsett facility. Squares containing different volumes of HOOPS crude oil and emulsified oil were aimed to create different thicknesses of each oil type if oil were to spread evenly in the squares. Unfortunately, due to oil heterogeneity even distributions of surface oil within the squares were impossible even without wind. When wind was blown from one

direction, oil may usually pile up in the square, creating a horizontal gradient. This makes it only possible to treat the squared oil as a whole with an equivalent mean thickness. Both clean Sargassum and oiled Sargassum (oiled by either crude or emulsified oil) were set in the squares. There is one square containing clean water to serve as a reference. Figure 6a shows a sample image of the experimental set up.

3) Multi-band camera Setup

The initial intension was to fly the UAS mounted with the multi-band and thermal cameras over the experimental setup above. However, during the experiment, flying any UAS was not permitted. Therefore, the UAS mounted with the cameras was put on a fixed platform to view the squares from directly above. Figure 7 shows the UAS setup over the squares.

Figure 7. UAS at Ohmsett.
UAS mounted on a crane at Ohmsett with the sensors looking towards the squares on the tank.

4) Calibration measurements by the SR-1900 spectroradiometer

Hyperspectral reflectance of the experimental squares was measured with the SR-1900 spectroradiometer in order to calibrate the concurrently collected camera images (Figure 8). In additional, hyperspectral reflectance was also collected from a reference plaque (Figure 9a) and some stable targets such as thick oil emulsion, thick crude oil, water on bare bottom, and water on tarp (Figure 8d). Because the solar illumination condition may change in a few minutes due to cloud cover, USF LICOR cosine collectors (Figure 8e) were used to record the downwelling solar irradiance continuously. The LICOR instruments measured downwelling irradiance from 350 nm to 850 nm at an interval of 5 nm.

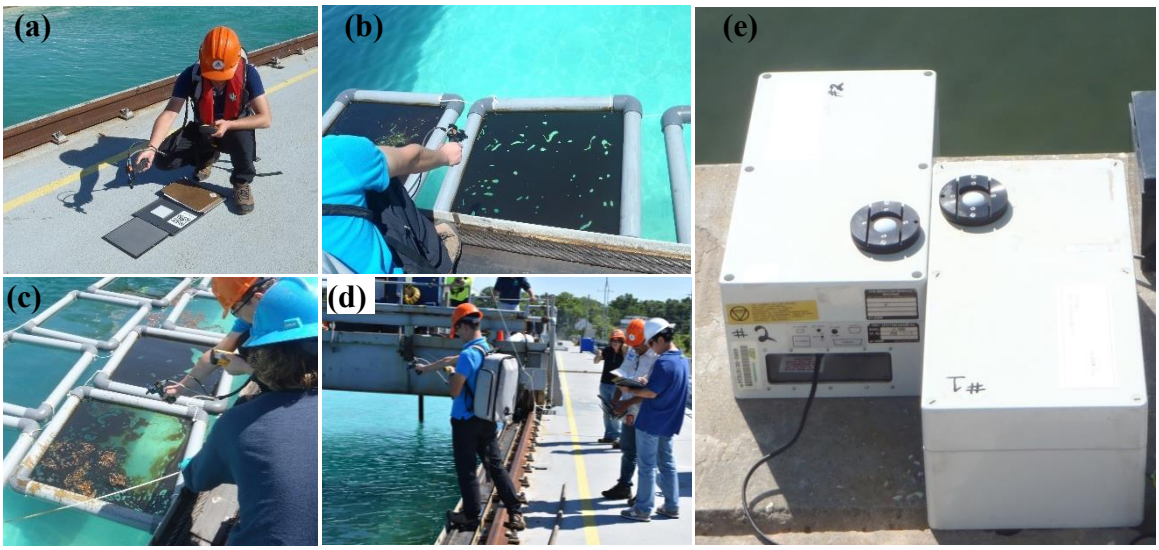

Figure 8. Radiometric calibration.
Hyperspectral reflectance of different targets was collected using the SR-1900 spectroradiometer during the Ohmsett experiment to calibrate the camera images. (a)-(d) Photos showing hyperspectral reflectance measurements.; e) USF LICOR cosine collectors were used to record the downwelling solar irradiance continuously in order to account for changing sky conditions between different measurements.

4. Results

4.1 Literature review: interpretation of oil-water spatial and spectral contrasts

Many features on the ocean surface can have broadband reflectance responses that make spectral discrimination difficult or impossible. In contrast, pure oil has narrowband reflectance signatures (Figure 2a; Lammoglia and Filho, 2011) in the NIR–SWIR spectral range due to combinations of organic molecules and compounds : (a) 1390/1410 nm due to O–H first overtone and C–H combinations first overtone; (b) at 1720–1730 nm from the combination of the CH3 and CH2 stretching and the combination of symmetric and asymmetric CH2 stretching; (c) at 1750–1760 nm, overtone of the CH2 vibration; (d) at 2310 nm, due to the combination of the CH3 asymmetric axial deformation with the CH3 symmetric angular deformation; (e) at 2350 nm, yielded by the combination of the CH3 symmetric axial deformation and the CH3 symmetric angular deformation; (f) at 1190/1210 nm some oil presents subtle spectral features as second overtones of C–H. In their experiments, Lammoglia and Filho (2011) did not find narrowband diagnostic features in the visible wavelengths.

The narrowband oil signature (Figure 2b; Clark et al., 2010) in the SWIR wavelength was observed from the DWH oil–water emulsion samples. With 60:40 oil–water mixing ratios, reflectance in the NIR–SWIR wavelengths also increases within increased oil thickness, and so do the line depths in the SWIR wavelength corresponding to the C–H compounds. These features (enhanced reflectance in the NIR–SWIR and C–H line depth) serve as an indicator of oil emulsion, and their magnitudes can be used to infer oil thickness for fixed oil–water mixing ratios (Clark et al., 2010). Note that compared to the NIR–SWIR wavelengths, there are negligible changes in the visible wavelengths, especially in the blue–green.

In contrast to the Clark et al. (2010) measurements, the laboratory experiments of Wettle et al. (2009) led to different results. The Gippsland crude showed no reflectance change in the NIR–SWIR wavelengths but monotonically decreased blue–green reflectance with increasing oil thickness (Figure 2c). This is understandable because when crude oil is not emulsified, the high absorption and relatively low scattering in the short wavelengths lead to the reflectance shapes shown in Figure 2c. In the same experiment, the Australian northwestern shelf light condensate showed no apparent reflectance change with increasing oil thickness, because this type of oil is

nearly transparent (e.g., ~100% light transmission from 400 nm to 1000 nm at a thickness of 200 μm, Wettle et al., 2009).

Wettle et al. (2009) experimental results are consistent with some of the experiments in Byfield (1999), where Gullfax crude shows decreased reflectance with increasing oil thickness when oil is on artificial seawater (Figure 2d). What is different is that such decreased reflectance also occurs in the NIR. When oil is put on real seawater, the same crude oil first shows decreased reflectance with increasing oil thickness, but then increased reflectance with increasing oil thickness (Figure 2e). Although the reason is not clear, the former reflectance decrease might be because the introduced higher reflectance from oil doesn't compensate the suppressing effect of surface oil Fresnel reflection on signal from the water column, as oil's reflection spectra are not changing much when thick enough (Figures. 2d&2e).

Overall, these laboratory experiments suggest that, at least in principle, when crude oil is non-emulsified, reflectance changes mainly occur in the blue–green wavelengths where reflectance decreases with increasing oil thickness; when oil is emulsified, reflectance changes mainly occur in the NIR–SWIR wavelengths where reflectance increases with increasing oil thickness. These observations may form the basis to interpret remote sensing imagery.

When similar experiments are conducted outdoors in a more realistic environment under ambient sunlight, different water types and illumination conditions may cause results to differ. Svejkovsky and Muskat (2006) measured Arabian Medium Crude oil in Oceanside Harbor, California, and found that reflectance initially increased then decreased with increasing oil thickness (Figure 2f). Reflectance of oil films in the visible wavelengths is generally lower than that of background water, with green wavelengths showing the largest changes with increasing oil thickness. This is possibly because unlike clear waters in laboratory experiments, turbid waters in a natural environment often have reflectance maximum in the green wavelengths because of strong absorption of phytoplankton and/or colored dissolved organic matter in the blue wavelengths and strong absorption of water molecules in the red and NIR wavelengths. An increase in oil thickness will thus "dampen" the green reflectance more than in other wavelengths. Note that thin films in this experiment show higher reflectance than water (Figure 2f). We believe this is caused by increased Fresnel reflectance at the surface of the oiled water, which is not compensated for by oil absorption because the oil is very thin.

4.2. Calibration of the multi-band imaging camera

After the March 2018 experiment, image pixel values from the Micasense imaging camera were calibrated to the SR-1900 measured reflectance through three steps: the factory calibration, field calibration, and the current measurement of the reference plaque.

Factory calibration was used to calibrate the raw pixel value from the Micasense camera to radiance using the following equation:

$$L=V(x,y)*a_1/g*(p-p_BL)/(t_e+a_2\ y-a_3\ t_e\ y) \quad (1)$$

where p is the normalized raw pixel value, pBL is the normalized black level value, a1 a2, a3 are the radiometric calibration coefficients, V(x, y) is the vignette polynomial function for pixel location (x, y). te is the image exposure time, g is the sensor gain setting, x and y are the pixel column and row numbers, respectively. L is the spectral radiance in W/m2/sr/nm.

The factory calibrated radiance was then compared to radiance measured by the SR-1900 spectroradiometer during the beach calibration experiment when the imaging camera and the SR-1900 measured the same reference plaque at the same time. The factory calibrated radiance was then further calibrated to the SR-1900 measured radiance using the coefficients from Figure 9 for the five Micasense bands.

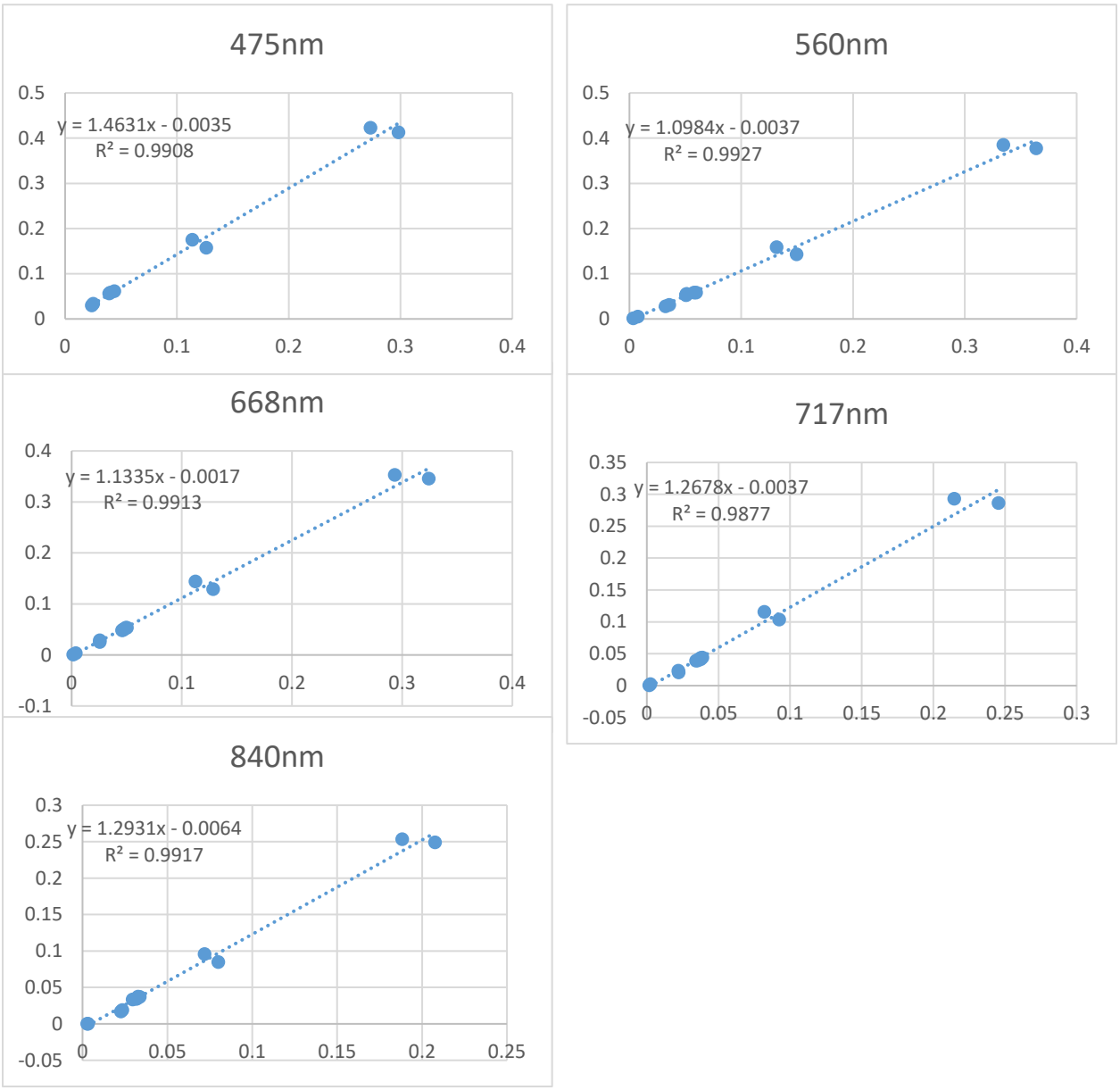

Figure 9. Calibration coefficients.
Calibration coefficients to convert factory calibrated Micasense camera radiance (x-axis) to SR-1900 measured radiance (y-axis). The calibration was performed for all 5 Micasense bands.

Finally, the derived radiance from the Micasense camera was then calibrated to reflectance using measurements from the reference plaque. As an example, Figure 10 shows such derived reflectance images from the Micasense camera, where sample reflectance spectra of two pixels of water and oil emulsion, respectively are also shown in Figure 11. In this example, while the

water reflectance shows typical low values in the NIR wavelengths due to strong water absorption, reflectance of the oil emulsion shows significantly elevated value in the NIR, consistent from those reported in the literature.

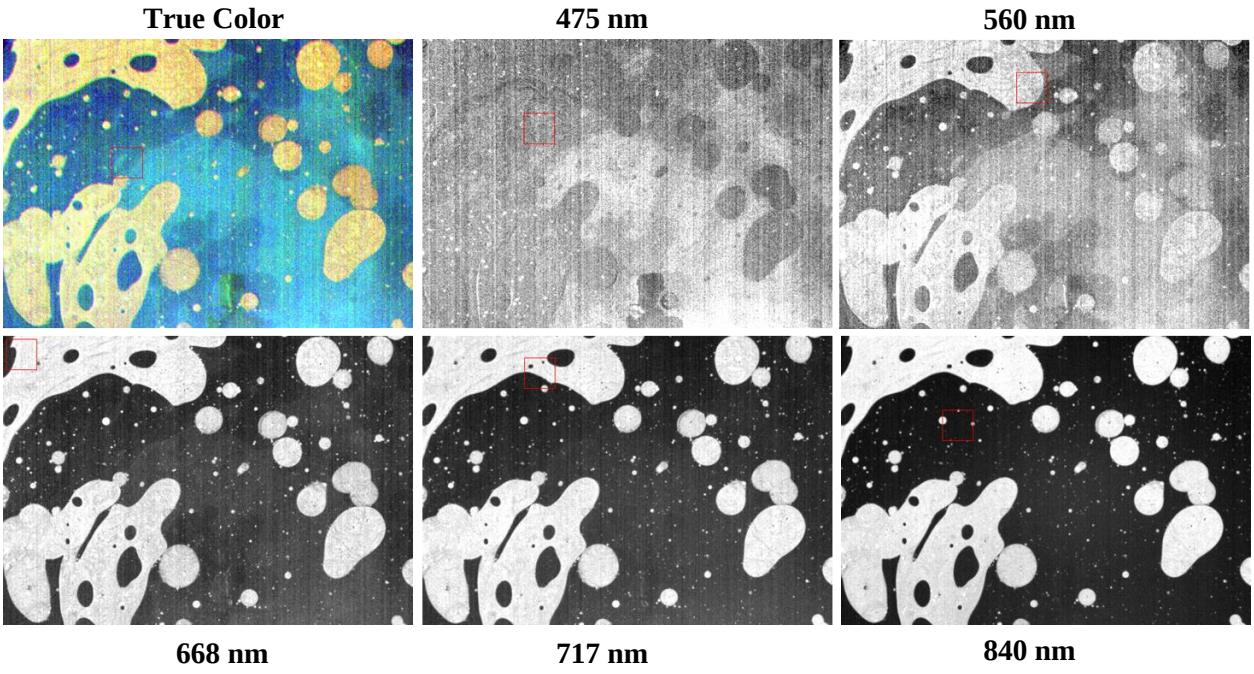

Figure 10. Calibrated reflectance images
Calibrated reflectance images from the multi-band Micasense camera, together with the true color image shown on the top left. The images were taken from the USF oil tank experiment where the equivalent mean thickness of the ANS oil emulsion was 750 µm.

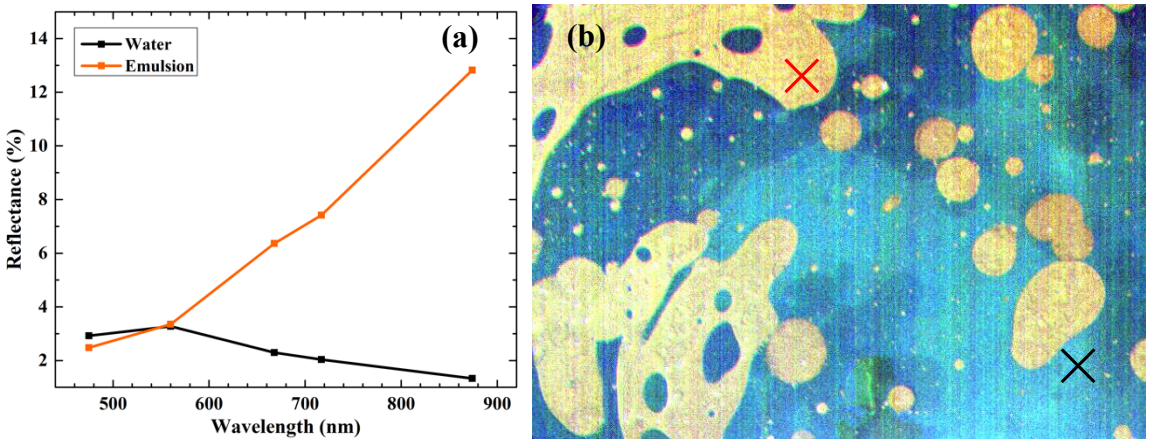

Figure 11. Reflectance spectra of a water pixel
a) Reflectance spectra of a water pixel and an oil emulsion pixel from the multiband Micasense camera (b).

4.3 Results from the USF oil tank experiment

4.3.1. Contrasting features from different bands

The experiment shows dramatically contrasting images among different camera bands because different wavelengths respond to oil-on-water differently. Figure 12 shows an example where the contrast can be clearly visualized. For this particular example where the equivalent mean oil thickness is 100 um, oil-water spatial contrast is higher in the NIR bands than in the blue-green bands, consistent from those reported in Clark et al. (2010). Similarly, the thermal images also show high spatial contrast, indicating their effectiveness in detecting thick oil emulsions.

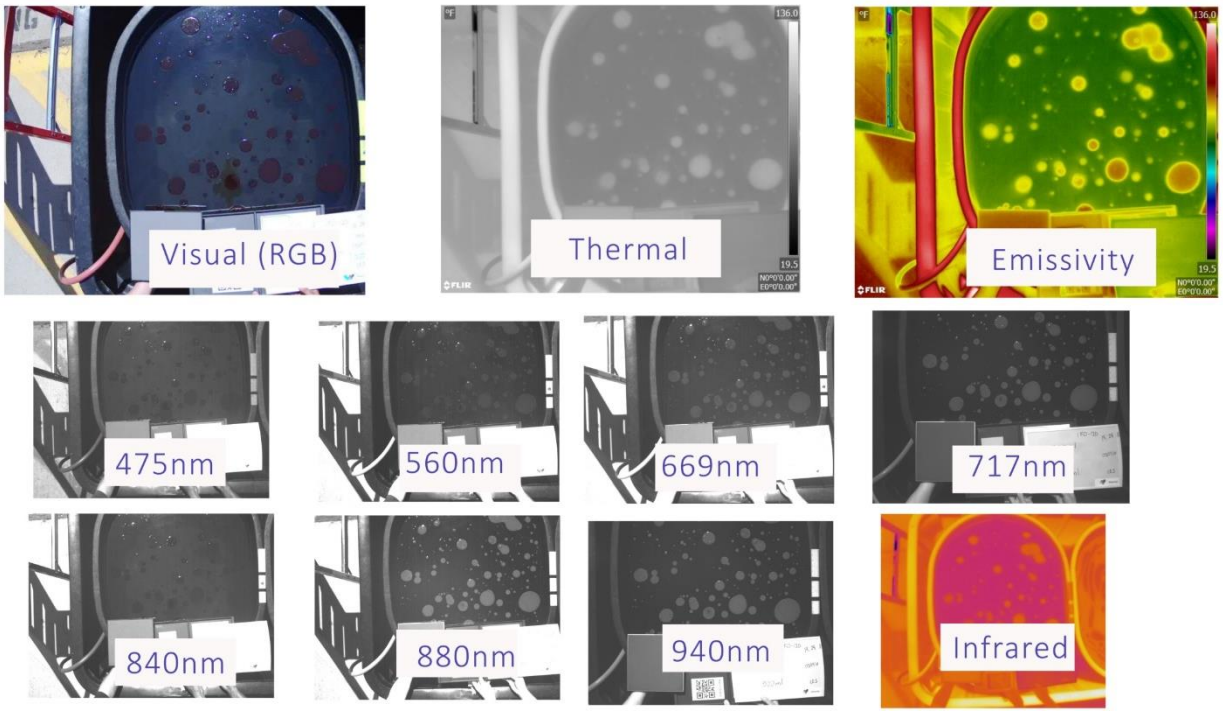

Figure 12. Sample images of oil emulsions
Sample images of oil emulsions at an average of 100um thickness from the multi-band cameras.

4.3.2 Oil heterogeneity and oil-water classification

Oil emulsions were not uniformly distributed in the tank due to their high viscosity, and they actually formed scattered patches even under calm conditions (Figure 13a). The scatter patches varied in size, from several millimeters to several centimeters. When the spatial resolution of remote sensing imagery is sufficient to resolve these patches, such as shown in this example, a supervised classification based on the spectral contrast between oil and water pixels could

classify the pixels very well (Figure 13b). However, if the resolution of remote sensing imagery is not sufficient, all these oil and water patches may be covered in just one pixel, making it difficult to interpret the spectral and spatial contrast.

Because of such a high heterogeneity, the actual thickness in an oil patch may be significantly different from the oil volume-calculated mean oil thickness. Indeed, the oil occupied surface area was estimated from the supervised classification result, which was then used with the total oil volume to calculate the realistic oil thickness assuming all oil patches had the same oil thickness. For comparison, oil thickness was also calculated as the total volume divided by the total tank area. In both approximations, oil thickness increased with oil volume, as shown in Table 2.

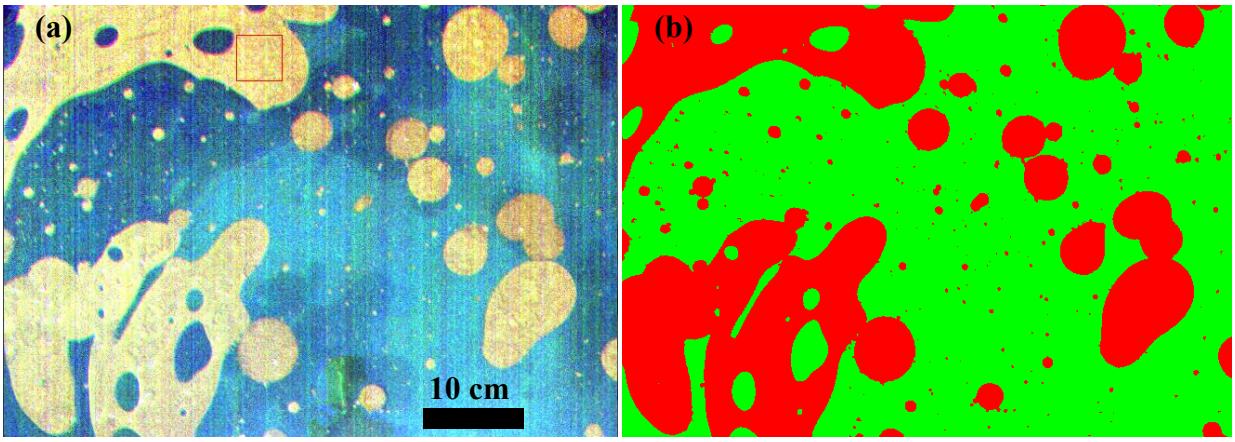

Figure 13. Oil emulsion test.
Oil emulsion distribution was not uniform in the water tank but very patchy. The example here shows a) true color image of oil emulsion from ANS with an equivalent mean thickness of 750 μm and b) classification of oil emulsion pixels and water pixels after a supervised classification (using maximum likelihood).

Table 2 Oil thicknesses tests.

Oil thickness from oil emulsions in the water tank calculated using two methods. the first column is the thickness calculated from the oil volume and tank area, representing the equivalent thickness if oil were evenly distributed on the entire tank surface. The last column is the realistic thickness calculated from the oil volume and oil-occupied area. a subset of the tank area was selected for separating oil emulsion from water to avoid shadows from the tank. As the tank shadows changed with time, the total number of pixels here are different for different scenarios

Thickness from volume (μm)	Emulsion (# of pixels)	Water (# of pixels)	Total # of pixels	Emulsion/total ratio	Realistic thickness(μm)
750	110,000	200,000	310,000	0.36	2,000
500	100,000	190,000	290,000	0.35	1,400
100	36,000	230,000	260,000	0.14	730
50	35,000	240,000	280,000	0.13	390
10	26,000	190,000	220,000	0.12	86
5	19,000	190,000	210,000	0.09	56

4.3.3 Hyperspectral response to oil thickness

Figures. 14, 15, and 16 show the reflectance response of increased oil thickness of the three oil types (ANS, HPS, IFO-120). Take ANS for example, when oil is very thin (≤1 μm), crude oil reflectance is higher than water in the visible wavelengths (400-700 nm, in Figure 14a). This is apparently due to enhanced Fresnel reflectance because oil has a higher refraction index than water. However, when oil becomes thicker (≥5 μm), there is a clear trend of decreased reflectance in the visible wavelengths with increased oil thicknesses until oil thickness reaches 100 - 500 μm. Compared to reflectance in the visible wavelengths, reflectance in the NIR and SWIR wavelengths shows minimal changes. These results agree well with previous laboratory studies of crude oil (Wettle et al., 2009). Most importantly, reflectance in the NIR and SWIR bands is very low (<0.5%, Figure 14a) for all thicknesses, which contrasts the enhanced NIR and SWIR reflectance of oil emulsions (e.g., 4% - 15% in the 1650-nm band with emulsion thicknesses from 50 to 750 μm, Figure 14b). Figure 14b shows increased reflectance in the NIR and SWIR wavelengths corresponding to thick emulsions. This agrees well with previous results by Clark et al. (2010). According to Table 2, the elevated reflectance in the NIR and SWIR

wavelengths is a result of both increased emulsion thickness and increased emulsion coverage in the tank.

Similar to the ANS example shown in Figure 14, the HPS and IFO-120 oil types show the same results in Figures 15 and 16, respectively. For crude oil, reflectance changes mostly occur in the blue-green wavelengths, with decreased reflectance when oil thickness increases. For oil emulsions, reflectance changes mostly occur in the NIR-SWIR wavelengths, with increase reflectance when oil thickness increases. These experimental results provide the fundamental basis to develop remote sensing algorithms to classify oil types (crude oil versus oil emulsion) and to estimate oil thickness.

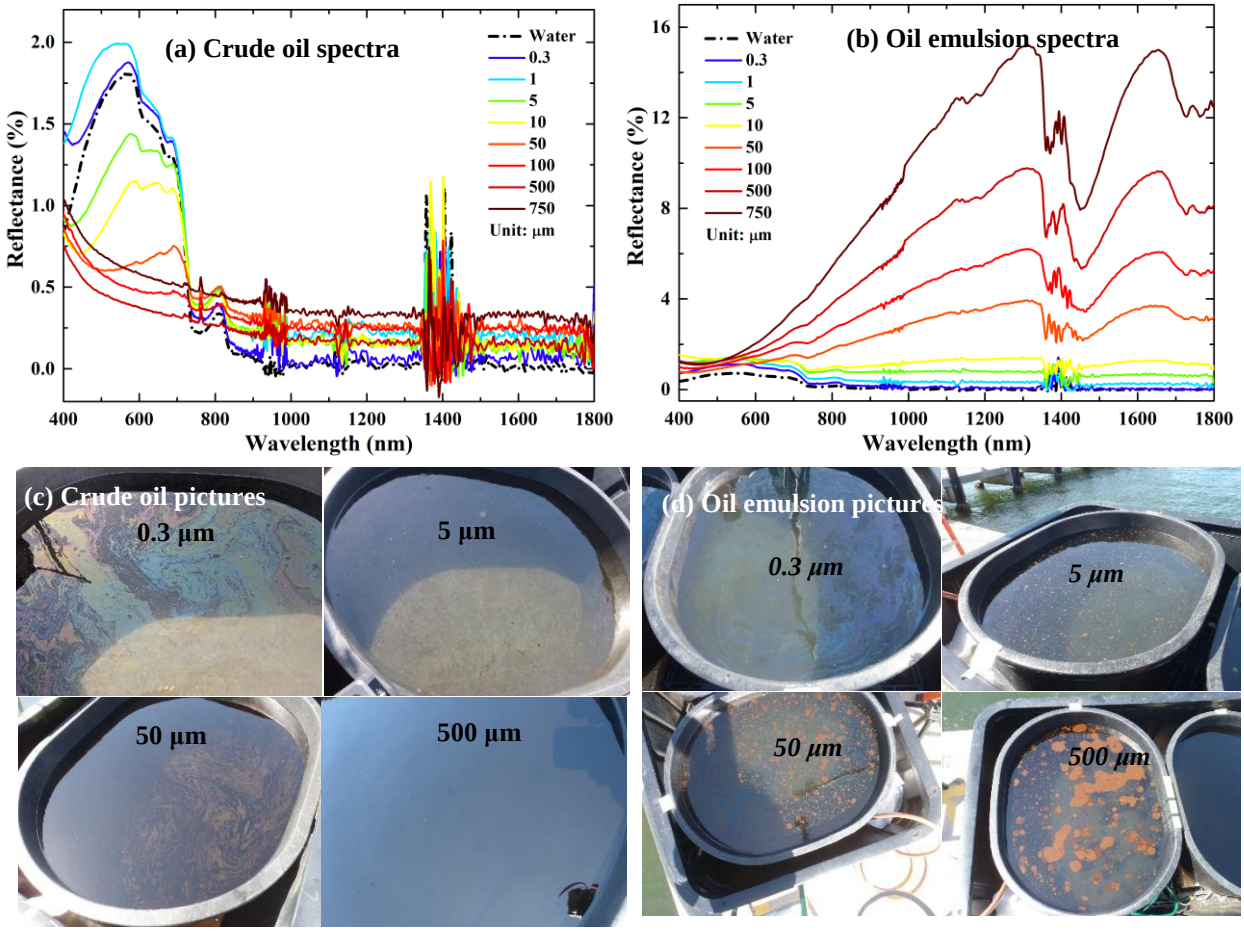

Figure 14. Reflectance of crude and emulsions

a) Reflectance spectra of ANS crude oil and b) ANS oil emulsion with various oil thicknesses in a water tank. Here thickness is calculated as the total volume divided by the area of the tank. Pictures showing c) crude oil and d) oil emulsion appearances with different thicknesses.

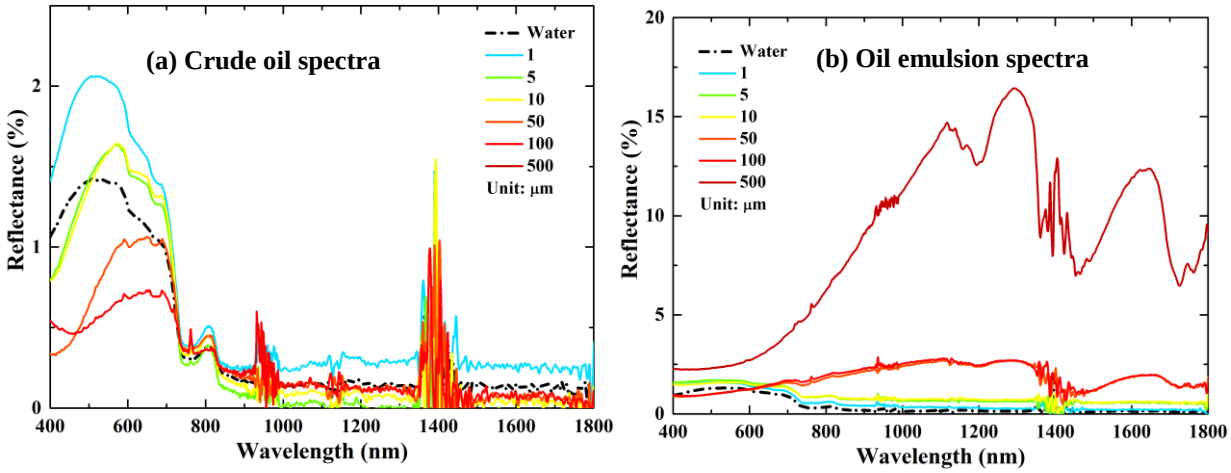

Figure 15. Crude and emulsion spectra test 1

a) Reflectance spectra of HPS crude oil and b) HPS oil emulsion with various oil thicknesses in a water tank.

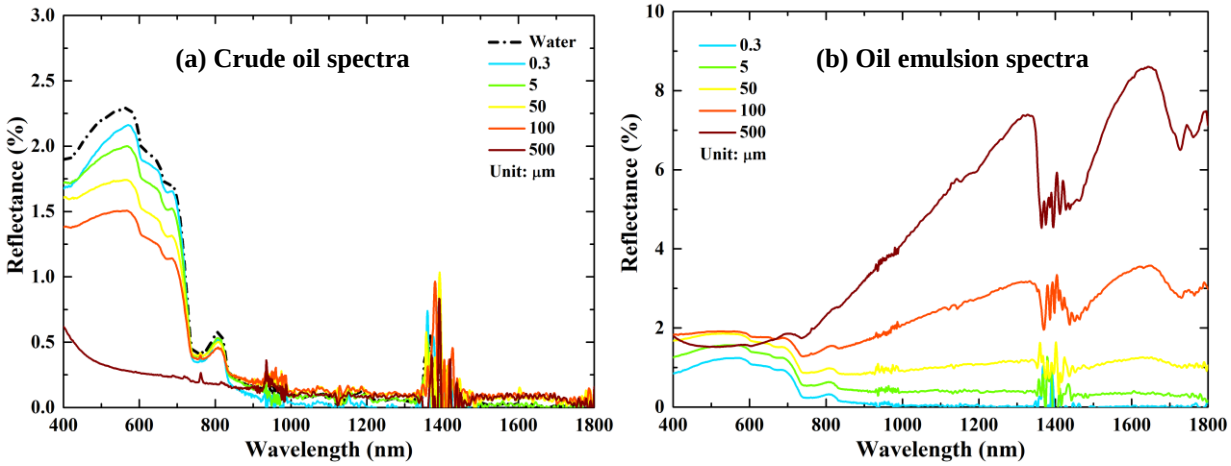

Figure 16. Crude and emulsion spectra test 2.

a) Reflectance spectra of IFO-120 crude oil and b) IFO-120 oil emulsion with various oil thicknesses in a water tank.

4.4 Results from the Ohmsett experiment

4.4.1. Imaging camera response

Figure17 shows the thermal response and multiband response of the multi-band cameras to different volumes of HOOPS crude oil and Sargassum in the squares. Similar to the USF water tank experiment, the oil in each square is not distributed uniformly but shows significant patchiness. Therefore, even if a mean thickness can be calculated from the known volume and surface area, the real thickness in the oil patch can be very different, making it difficult to associate the SR-1900 measured thickness with the calculated mean thickness. This is because it is unknown which exact oil patch the hand-held SR-1900 spectroradiometer was viewing.

Figure 18 shows another example from the HOOPS oil setup where the same observations can be made: oil in the square is not uniformly distributed but rather patchy.

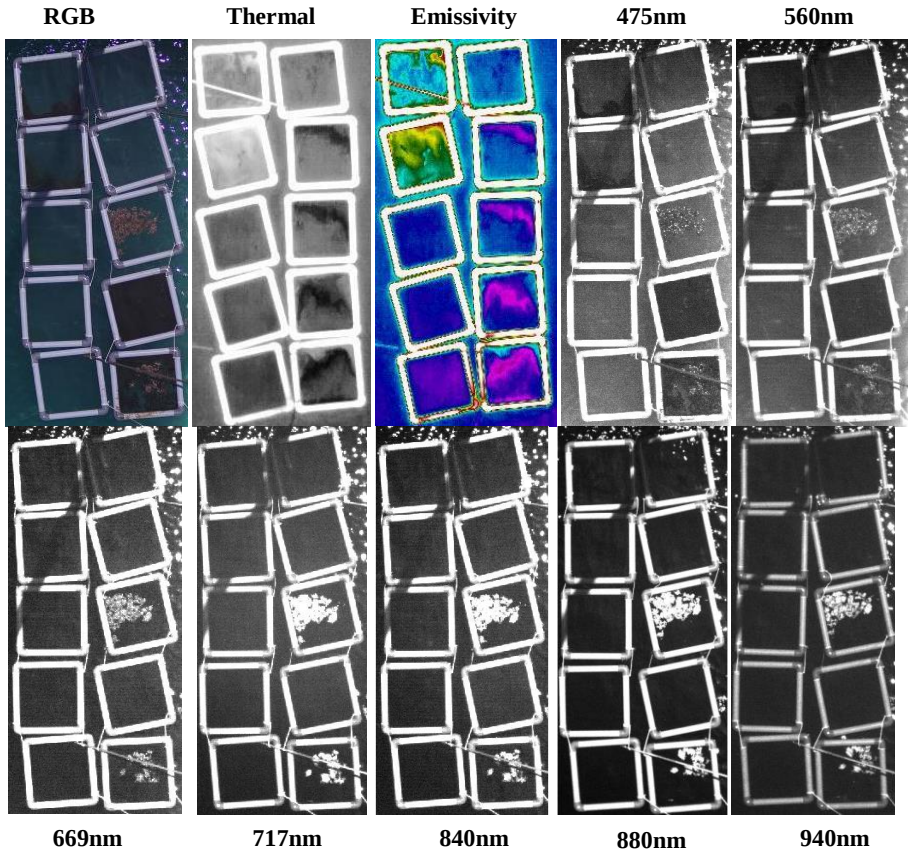

Figure 17. Grid of thicknesses squares at Ohmsett.
Thermal image and multi-band images of HOOPS crude oil and Sargassum setup shown in Figure 6a.

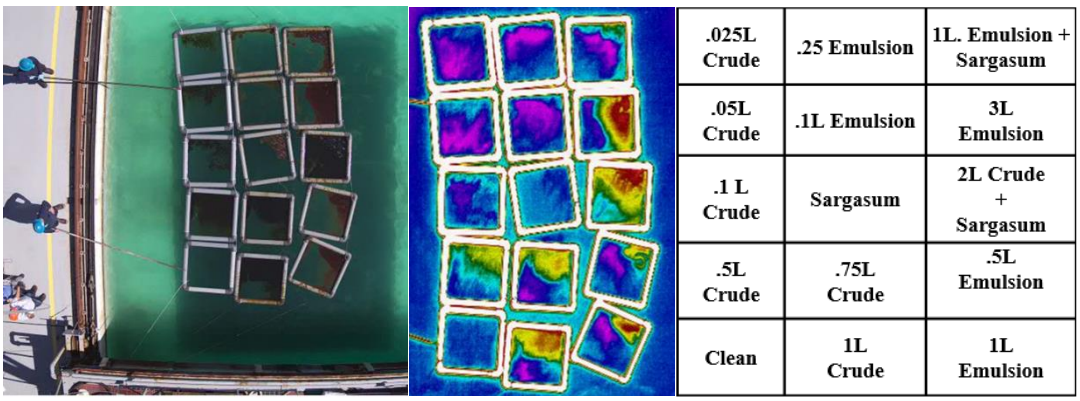

.025L Crude	.25 Emulsion	1L. Emulsion + Sargasum
.05L Crude	.1L Emulsion	3L Emulsion
.1 L Crude	Sargasum	2L Crude + Sargasum
.5L Crude	.75L Crude	.5L Emulsion
Clean	1L Crude	1L Emulsion

Figure 18. Grid of thicknesses squares at Ohmsett 2.
Square setup containing different volume of HOOPS oil emulsions, crude oil, and Sargassum. Left: RGB image of the setup; Middle: thermal images; Right: details of the setup in each square. Here 1 liter of oil corresponds to 1 mm thickness layer of oil in the square if oil spread evenly in the square; same applies to Figure 19 – Figure 22.

4.4.2 Image classifications

As shown above, oil emulsion and crude oil show different reflectance in the red, NIR and SWIR bands—oil emulsions have high reflectance in these bands while crude oil has very low reflectance (almost zero) in these bands. These observations can be used to develop algorithms to classify oil emulsions from crude oil. For example, of the square setup on June 14, 2018 (Figure 19), crude oil shows dark color in both the true color (R: 668; G: 560; B: 475 nm) and false color (R: 840; G: 668; B: 560 nm) images. Oil emulsions display reddish color in the true color image but brownish to yellowish color in the false color image. Sargassum appears as dark brownish in the true color image while but reddish color in the false color image. The same color appearance of the three different target types can also be found in the square setups in Figures 20, 21, 22.1, 22.2, and 22.3, respectively. Clearly, with a combination of true color and the false color images, crude oil, oil emulsion, and Sargassum can be differentiated and classified.

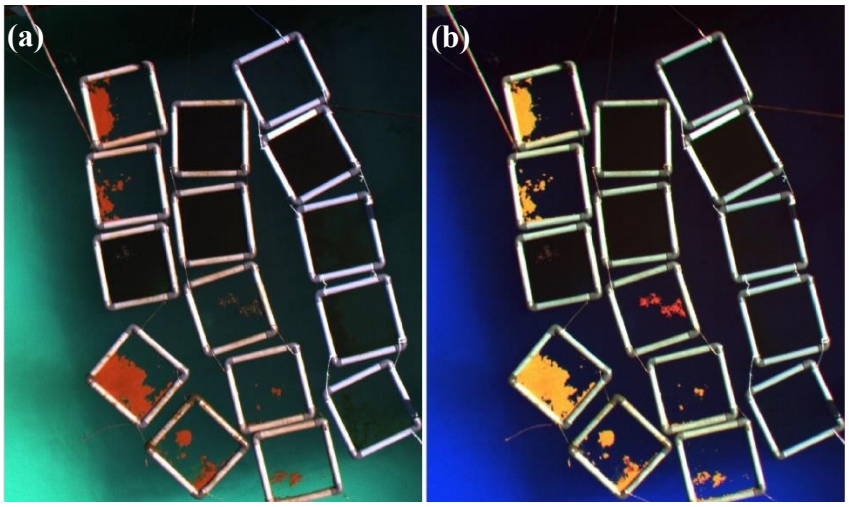

(c)		
1L Emulsion	1L Crude	Clear
.5L Emulsion	.75L Crude	.5L Crude
2LCrude + Sargassum	Sargassum	.1L Crude
3L Emulsion	.1L Emulsion	.05L Crude
1LEmulsion + Sargassum	.25L Emulsion	.025L Crude

Figure 19. Grid of thicknesses squares at Ohmsett 3.
a) True color (R: 668; G: 560; B: 475 nm) and false color (R: 840; G: 668; B: 560 nm) images from the multiband camera of the oil (HOOPS) square setup taken on June 14, 2018. c) Details of the setup in each square.

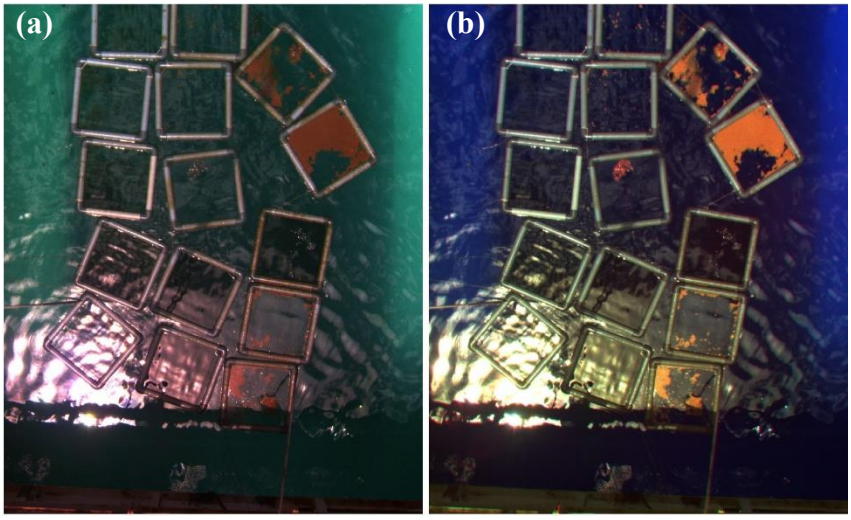

(c)		
.025L Crude	.25L Emulsion	1LEmulsion + Sargassum
.05L Crude	.1L Emulsion	3L Emulsion
.1L Crude	Sargassum	2LCrude + Sargassum
.5L Crude	.75L Crude	.5L Emulsion
Clear	1L Crude	1L Emulsion

Figure 20. Grid of thicknesses squares at Ohmsett 4.
a) True color (R: 668; G: 560; B: 475 nm) and false color (R: 840; G: 668; B: 560 nm) images from the multiband camera of the oil (HOOPS) square setup taken on June 15, 2018. c) Details of the setup in each square.

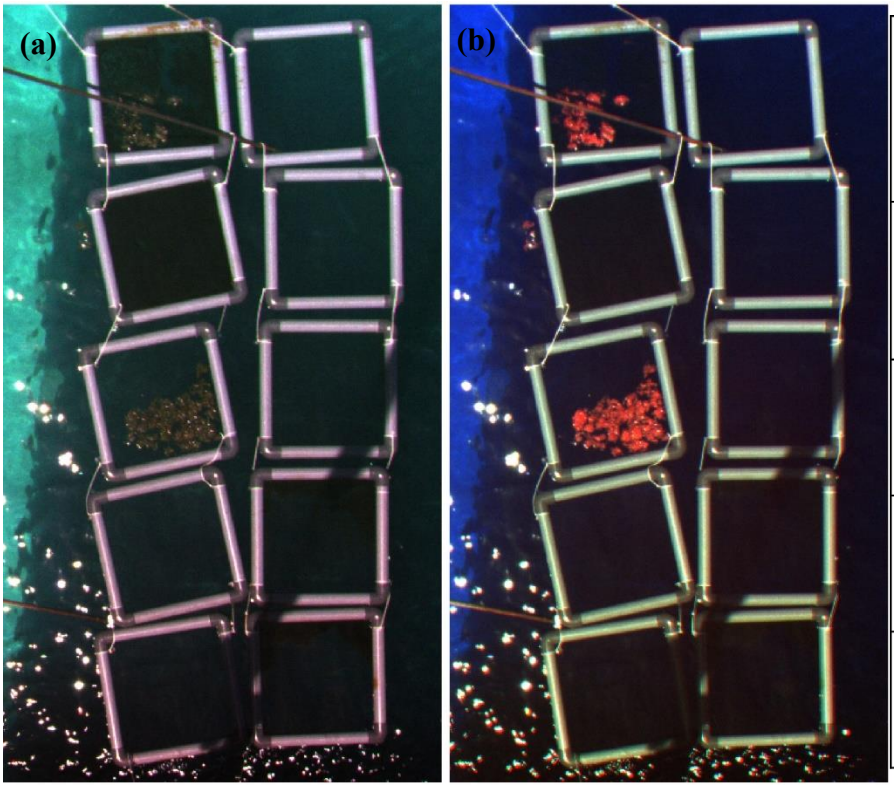

(c)	
.75L Crude + Sargassum	.01 Crude
1L Crude	.05 Crude
Sargassum	.1 Crude
.1L Crude	.25 Crude
Clear	.5 Crude

Figure 21. Grid of thicknesses squares at Ohmsett 5
a) True color (R: 668; G: 560; B: 475 nm) and false color (R: 840; G: 668; B: 560 nm) images from the multiband camera of the oil (HOOPS) square setup taken on June 12, 2018. c) Details of the setup in each square.

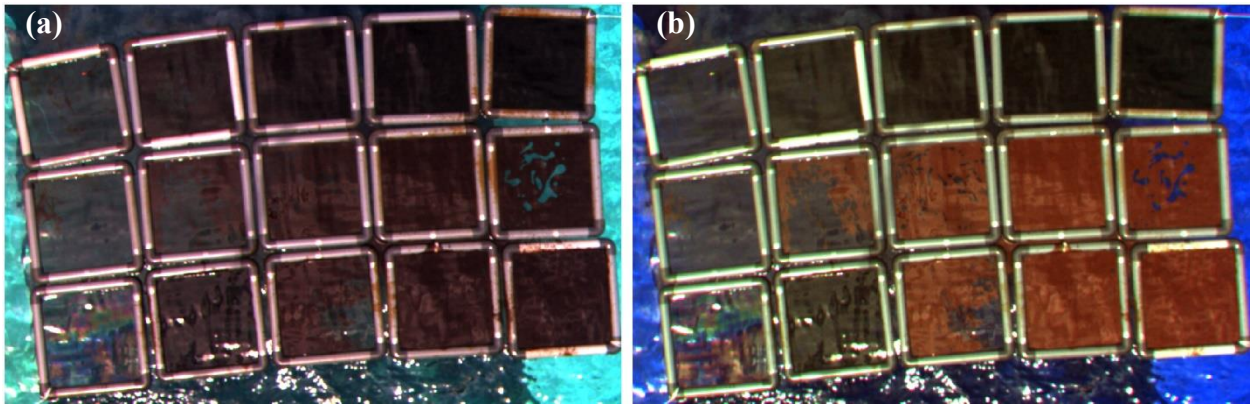

(c)

HOOPS Crude 0.1L	HOOPS Crude 0.5L	HOOPS Crude 1.0L	HOOPS Crude 3.0L	HOOPS Crude 5.0L
HOOPS Emulsion 0.1L	HOOPS Emulsion 0.5L	HOOPS Emulsion 1.0L	HOOPS Emulsion 3.0L	HOOPS Emulsion 5.0L
Sheen	ANS Crude 1.0L	ANS Emulsion 1.0L	ANS Emulsion 3.0L	ANS Emulsion 5.0L

Figure 22.1 Grid of thicknesses squares at Ohmsett 6.
a) True color (R: 668; G: 560; B: 475 nm) and false color (R: 840; G: 668; B: 560 nm) images from the multiband camera of the oil square setup taken on July 24, 2018. c) Details of the setup in each square.

Based on the emissivity contrast, the classification of the oil thickness can be achieved as shown on figure 22.2.

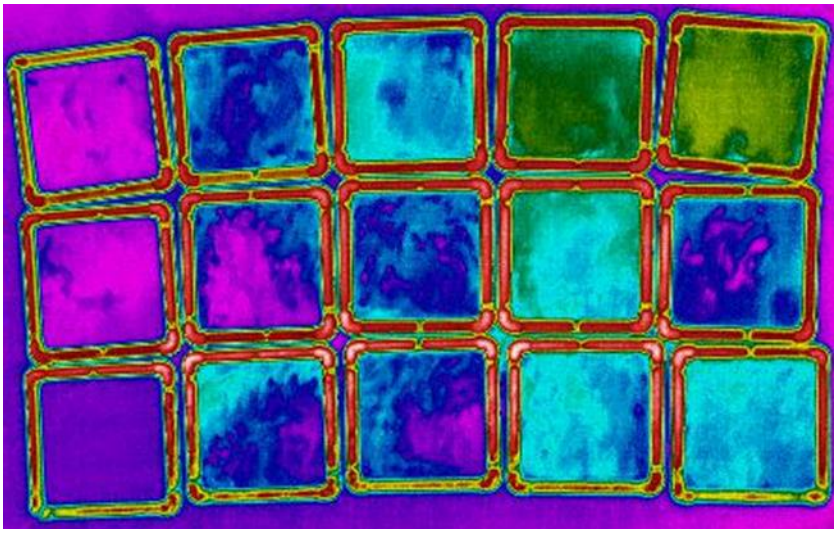

Figure 22.2 Emissivity Contrast for thickness classification.

We used the GPS and flight track information on the UAS to generate a projected still of the multispectral data. This was used to produce a oil thickness volume classification on near-real time. The map below (Figure 22.3) was generated as a demonstration at Ohmsett, nearly 25 minutes after the data was collected. This map was shown to BSEE, Ohmsett, and other personnel present during the experiment.

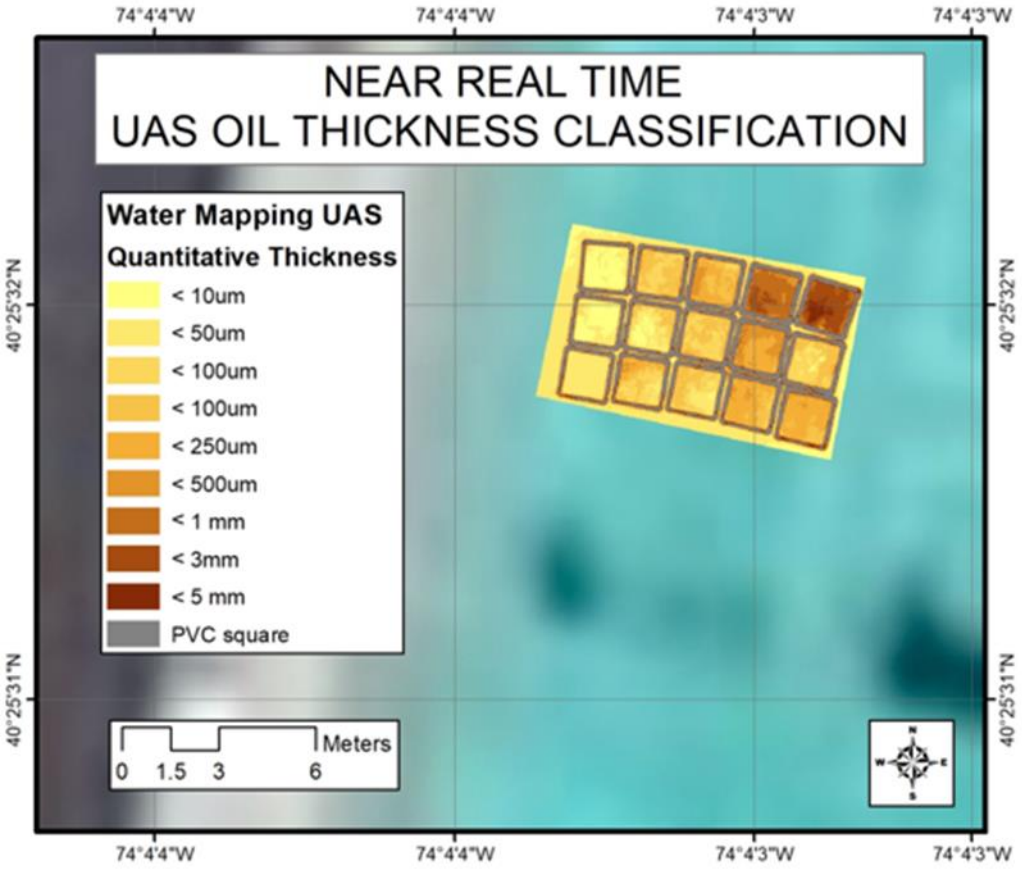

Figure 22.3 Demonstration of near-real time quantitative classification of oil thickness inside the Ohmsett tank.

4.5 Practical multiband algorithm for oil type classification and oil thickness estimation

Based on the above results, a three-step simple classification scheme was developed to classify oil type (crude oil versus oil emulsion) and relative oil thickness for each type using multiband images. Specifically, four bands are required for the practical method: blue (~470 nm), green (~560 nm), NIR (~860 nm), and SWIR (preferred, i.e., ~1612 nm). If there is no SWIR band

from the multiband sensor, the fourth band could be replaced by a red band (~645 nm) instead. These three steps are:

1) Determine and delineate oil pixels using spatial contrast on each pixel. A crude oil–water boundary was first determined through visual inspection. Then, a kernel (100x100 pixels for example, which is determined by slick size) was applied to each oil pixel to find all nonoil pixels within the kernel, from which mean and standard deviation of reflectance were calculated. If the oil pixel showed a difference (from water) of < 2*stdev in all bands, it was reclassified as a nonoil pixel.

2) Classify oil types from the delineated oil pixels into two types: emulsion and non-emulsion. If an oil pixel has a contrast (referenced against the nearest nonoil pixels) > 2*stdev of the nearest nonoil pixels in all the NIR and SWIR (or red) bands, it is classified as oil emulsion, otherwise it is classified as non-emulsion.

3) Estimate relative oil thickness for both oil types. Oil emulsion was quantified using the band ratio of SWIR (NIR) to blue: higher ratios indicate thicker oil. Non-emulsion was quantified also using the band ratio of SWIR (NIR) to blue: higher ratios indicate thicker oil, according to the spectral analysis above.

The three-step classification scheme (hereafter referred to as multiband approach) was applied to multiband data extracted from the hyperspectral AVIRIS data collected on 17 May 2010, with results shown in Figure 23. The classification results in Figure 23b agree well with the visual inspection of the RGB image in Figure 23a. To further evaluate the performance of the multiband approach, results from the USGS hyperspectral approach by Clark et al. (2010; hereafter referred to as the USGS approach or hyperspectral approach) are presented in Figures 23c and 23d.

Figure 23c shows that the USGS approach resulted in similar spatial distribution patterns of oil emulsion as those from the multiband approach (Figure 23b), yet the former has smaller footprint. This is because the USGS approach (2010) was designed to map only thick emulsions as opposed to thin emulsions and non-emulsions, therefore representing a conservative estimation. In contrast, the multiband approach not only identified the same pixels of thick oil emulsions, but also detected thin oil emulsion and non-emulsion pixels, as shown in Figures 23b and 23d. A total of 14205 AVIRIS pixels (Table 3) were classified as oil emulsion by the multiband approach, 2616 of which agreed with the USGS-derived oil emulsion pixels (Figure

23c). These 2616 pixels actually represent >99.8% of all oil emulsion pixels identified by the USGS approach (Table 3). The reflectance spectra of these 2616 pixels display typical features in the NIR and SWIR bands for oil emulsion (Figure 23d). Yet the oil emulsion pixels identified only by the multiband approach also show similar features in the NIR and SWIR although at lower magnitudes ("Additional emulsion: this study" in Figure 23d), suggesting the validity of the multi-band approach in identifying both thick oil emulsions and thin oil emulsions. Those spectra features are clearly different from the non-emulsified oil pixels (Figure 23d), whose spectra are close to water reflectance in the NIR and SWIR bands but different from water reflectance in the blue-green bands. These results agree well with the spectral characteristics determined from laboratory measurements in the absence of sun glint, thus confirming the validity of the multiband approach in classifying oil types.

Table 3 AVIRIS pixels classification.

Comparison between numbers of AVIRIS pixels classified as three types (emulsion, non-emulsion, and water) from the multiband approach proposed in this study and number of oil emulsion pixels determined from the USGS hyperspectral approach (2010) for the AVIRIS image shown in Figure 23.

AVIRIS Pixel Type	# of Pixels (this study)	# of USGS oil emulsion pixels classified as the three types in this study
Emulsion	14205	2616
Non-Emulsion	16021	2
Water	329618	3
Total	359844	2621

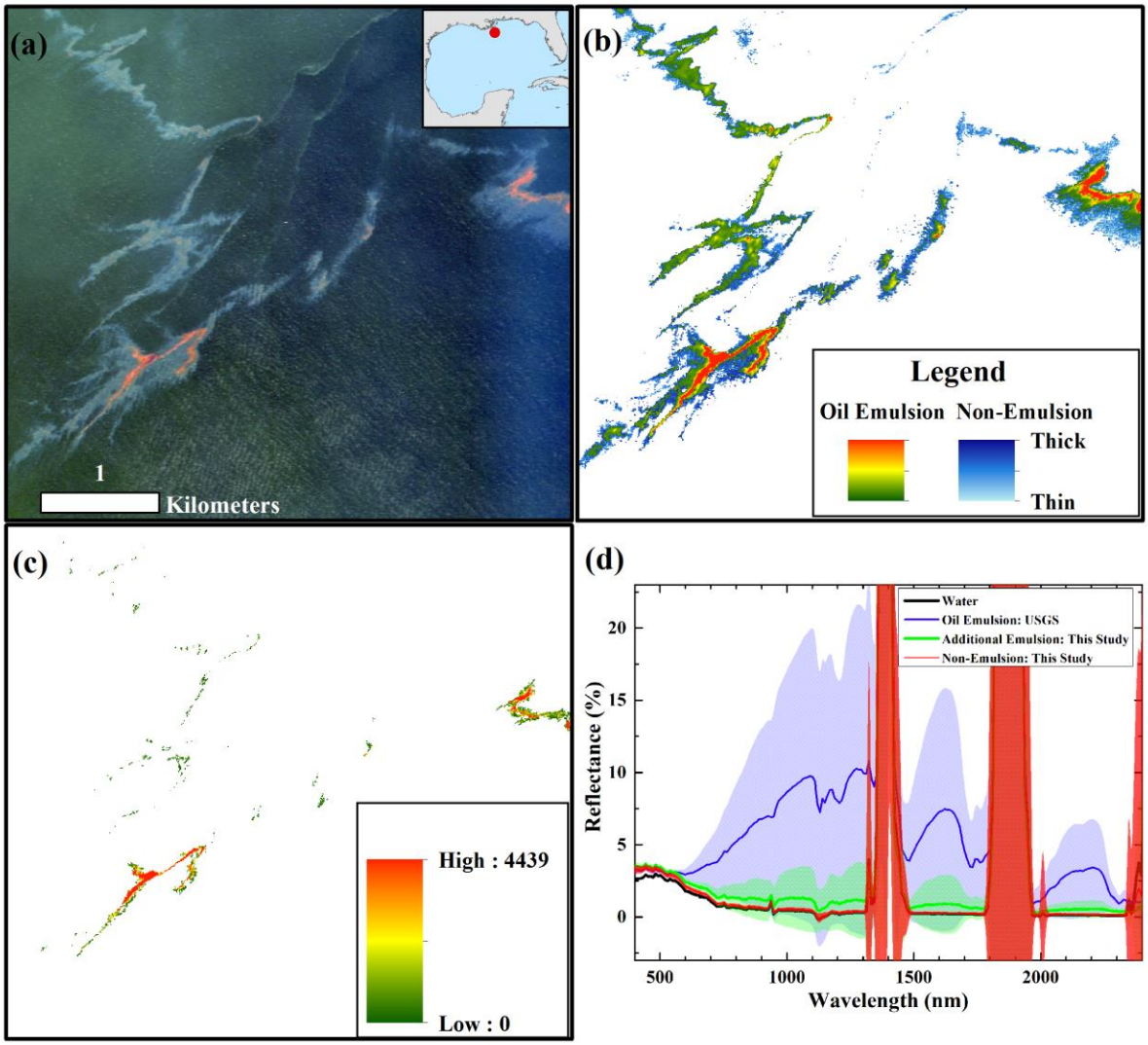

Figure 23. Application of multispectral imaging with AVIRIS.
Demonstration of a three-step classification scheme to determine oil type and thickness using selected AVIRIS bands. a) AVIRIS image taken on 17 May 2010. The RGB (R: 638nm, G: 550nm, B: 463nm) image shows the color difference between oil emulsion and non-emulsion, with inset figures showing the location of AVIRIS image in the GoM; b) Multiband classification results of oil emulsion and non-emulsion and their relative thickness; c) Oil emulsion determined from the hyperspectral data using the USGS approach (2010). Here the oil emulsion thickness was calculated as oil volume divided by the pixel size (7.6x7.6 m2). The entire maps is openly available at https://pubs.usgs.gov/of/2010/1167/downloads/figure16c-geotiff.tif; d) Mean and standard deviation spectra of several classified pixels, using both the USGS approach and the approach developed in this study. "Oil Emulsion: USGS" indicates the oil pixels identified by the USGS hyperspectral algorithm by Clark et al (2010). "Additional emulsion: this study" and "Non-emulsion: this study" indicate the oil pixels identified by the multi-band algorithm developed in this study which were not identified by the USGS algorithm.

The three-step practical approach was also applied to multiband sensors such as MODIS under negligible sun glint conditions, where the MODIS-derived relative thickness and AVIRIS-derived oil thickness show similar spatial distribution patterns (Figure 24).

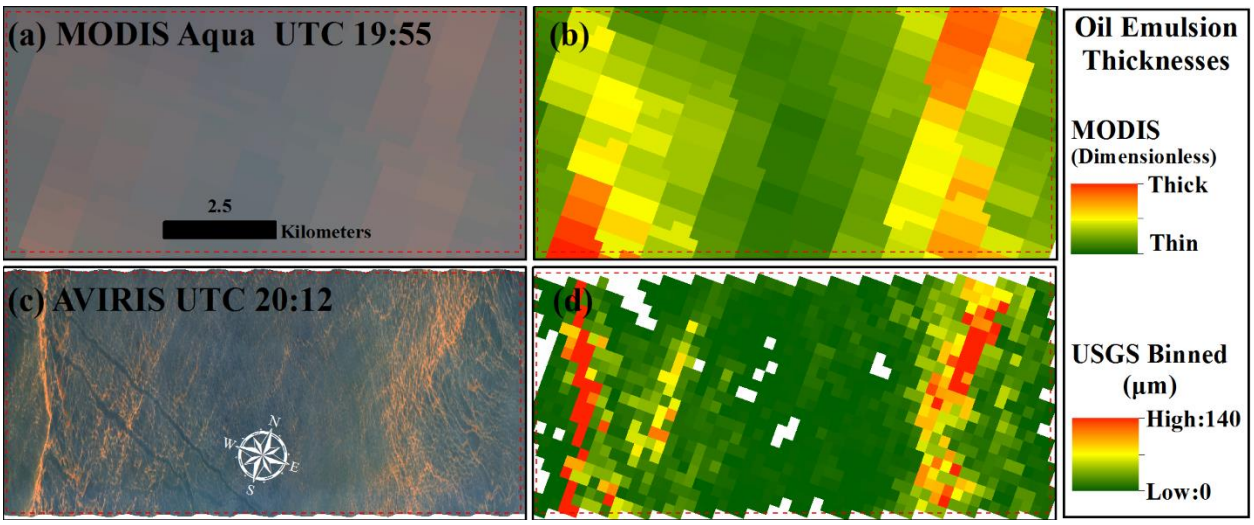

Figure 24. Comparison between multi-band MODIS and hyperspectral AVIRIS.
Comparison between multi-band MODIS (top) and hyperspectral AVIRIS (bottom) for their derived oil thickness from the classified oil emulsion on 17 May 2010. The relative oil thickness image (b) was derived from MODIS multi-band Rrc data (469, 555, 645, and 859 nm) using the methods proposed in this study. Accordingly, the band ratio of 859-nm to 469-nm was used in quantifying the oil emulsion thickness. The absolute oil thickness image (d) was derived from AVIRIS hyperspectral data by the USGS (2010) after binning to 250-m resolution. The MODIS bands have nadir resolutions of 250-500 m, but for this scan-edge image the resolution is about 1-2 km.

5. Lake Washington Oil Spill

We tested the multispectral array of sensors during the Lake Washington Oil Spill, which started on December 8th of 2018. This spill was reported by the U.S. Coast Guard as an equipment failure on the wellhead casing in Lake Washington/Rattlesnake Bayou. This event presented an excellent opportunity for testing our multispectral UAS on a real setting scenario, as we were aware of possible oil slicks with different thicknesses. These thicknesses ranged from thin sheens to actionable oil. Figure 25 is a report made by NOAA-NESDIS of the possible areas affected by the spill.

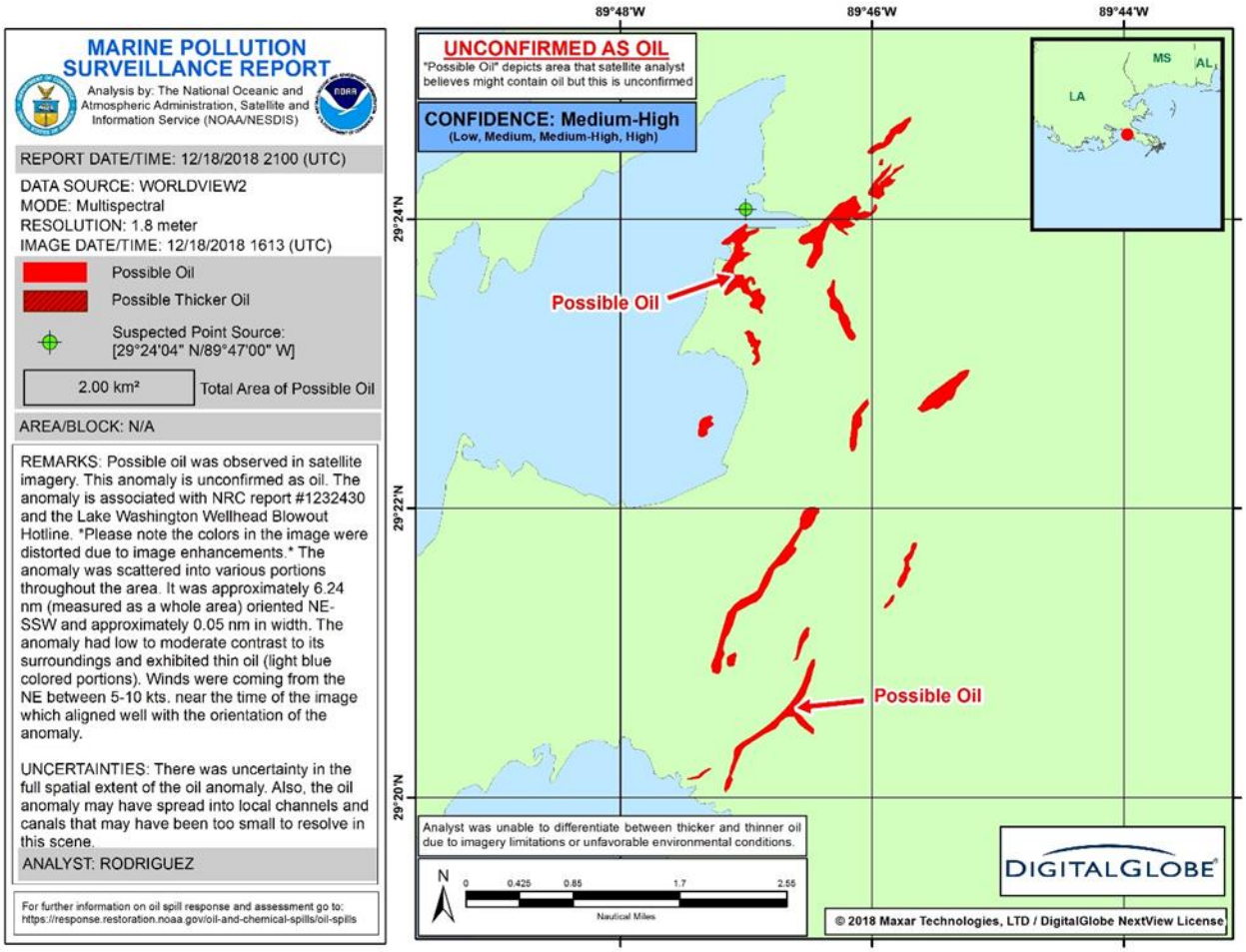

Figure 25. NOAA Marine pollution surveillance report.
This map was publicly released by NOAA-NESDIS as initial assessment of the oil distribution as interpreted by NOAA/NESDIS analysts after reviewing a satellite imagery captured by WorldView-2.

5.1 Initial Testing of equipment

We used the services from a local charter vessel company. We chartered low draft boat. This gave us access to the shallow areas where the spill was occurring. We arrived at the scene of the spill on December 10th, 2018. We were able to quickly identify areas where the thick floating oil could be present and proceeded to prepare our equipment for deployment. The first steps consisted on testing and calibration of the equipment. Tests consisted on aircraft flight checks, camera calibration, and real-time video system check. Figure 26 shows the UAS with all the multispectral sensors collecting a snapshot of the calibration panel.

Figure 26. Multispectral UAS system pre-flight calibration steps.
Here it shown the calibrated reflectance panel used for the multispectral sensor calibration.

As deployment preparation take place, Figure 27 (left) shows initial tests of the aircraft and camera systems. Multiple maneuvers are performed to ensure the proper performance of the aircraft. These tests are performed at low altitude (~30 ft) for optimal equipment performance. These tests consisted of real-time reviewing of high-resolution thermal and visual videos (Figure 27 right). This signal was received to the pilot's controller and then projected to a screen inside the cabin of the boat.

During this spill event, a massive amount of oil was observed floating on the surface of the area, which could be deleterious to the environment. The next series of photos is a collection of views from the high-resolution camera onboard of the UAS.

Figure 27. UAS Test.
Initial test of the UAS flights (left) and testing of the communication systems for flight control and multispectral cameras status. The panel on right shows a view of the controller for the aircraft.

The next figures are aerial views of the area of the spill. Figure 28 shows a heavy dark patch of oil drifting along rainbow sheen slicks around the small islands on the area. Figure 29 shows the thick patch of oil from a different angle. Multiple small islands were very close to the location of the thick oil. The examples of Figure 28 and 29 are oblique views from the UAS that are delivered on real time to the vessel. These views are collected at height of 400ft.

Figure 28 Aerial view of the oil spill. Oblique image collected at a height of 400 ft

Figure 29 Additional aerial view of the oil spill.
Oblique image collected at a height of 400 ft

We detected a thick patch of oil and proceeded to collect multispectral data with the UAS. Figure 30 shows a very heavy patch of crude our vessel passing through it. The UAS height at this point was still 400 ft. above sea level.

Figure 30 shows the vessel that we leased as its passing through a heavy thick patch of oil. We proceeded to collect multiple passes of multispectral data along the area of spill. Although the spill encompassed a larger area, we focused on collecting UAS data on areas where we could see a variation on the oil thicknesses.

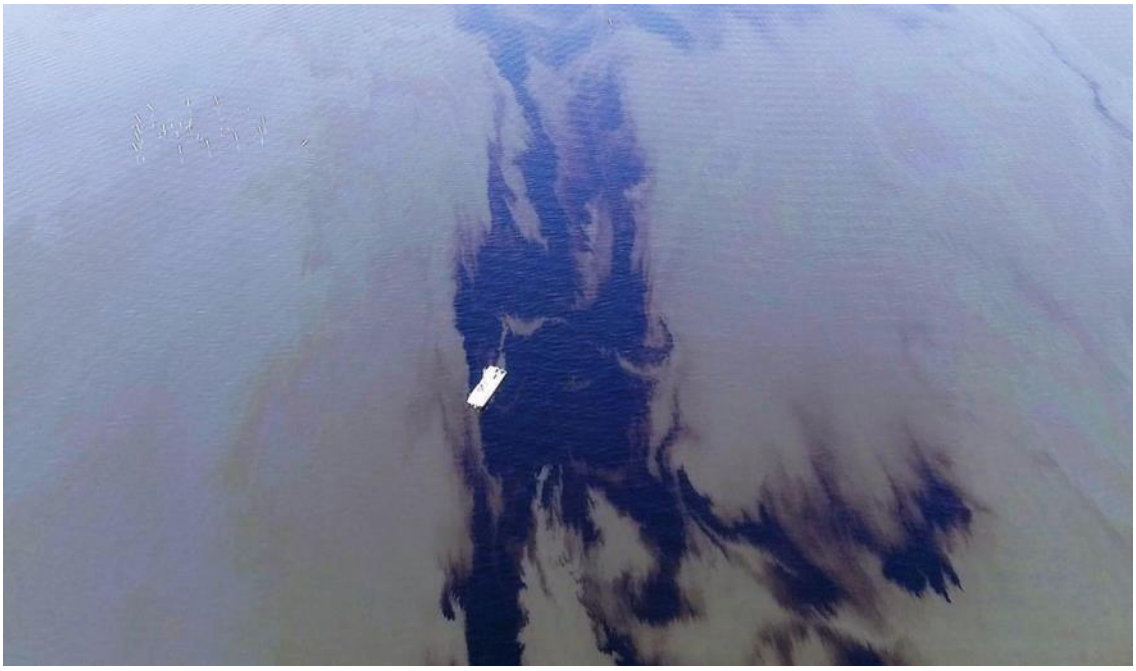

Figure 30 Detection of thick oil.
The vessels from where we were operating the UAS and collecting oil thickness measurements shows in the center of this aerial view.

The photo on Figure 31 shows an example of an absorbent pad that was used to get a reference of the aspect of the oil. Figure 31 shows a sample of oil collected by an absorbent pad on an area of heavy thick fresh oil.

Figure 31 Collection a sample with an absorbent pad

Figure 32 shows the floating thick oil as imaged from the deck of the boat. The reddish aspect of the floating oil suggests a degree of emulsification.

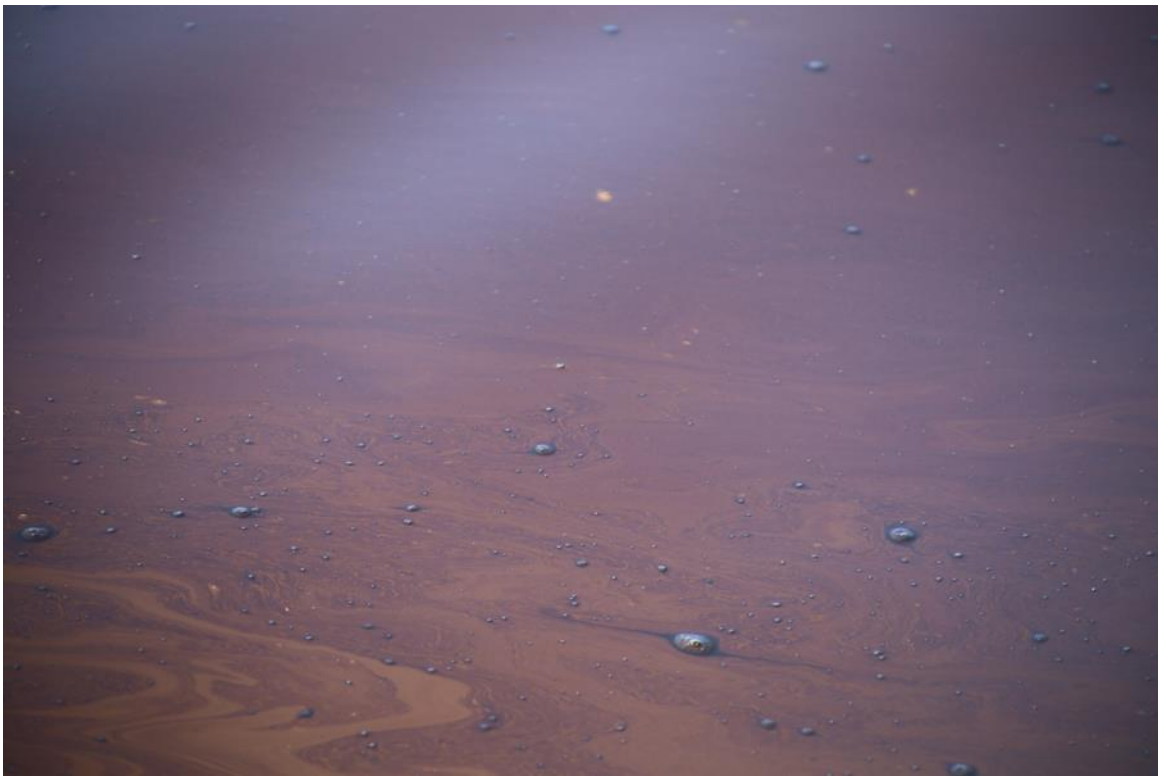

Figure 32 Floating thick oil during the Lake Washington Oil Spill

We also observed heavy thick emulsions that started to form approximately at 3 miles south from the wellhead's location. We proceeded to collect samples with our WM-OST for measurements of thickness (Figure 33). In total we collected 11 measurements of thickness across the slicks. All the measurements were collected during the UAS flight over the area, and a GPS log was created for each sample. Thickness samples were processed with our digital photography method. These thickness measurements are used to ground truth the thicknesses observed on the multispectral imagery.

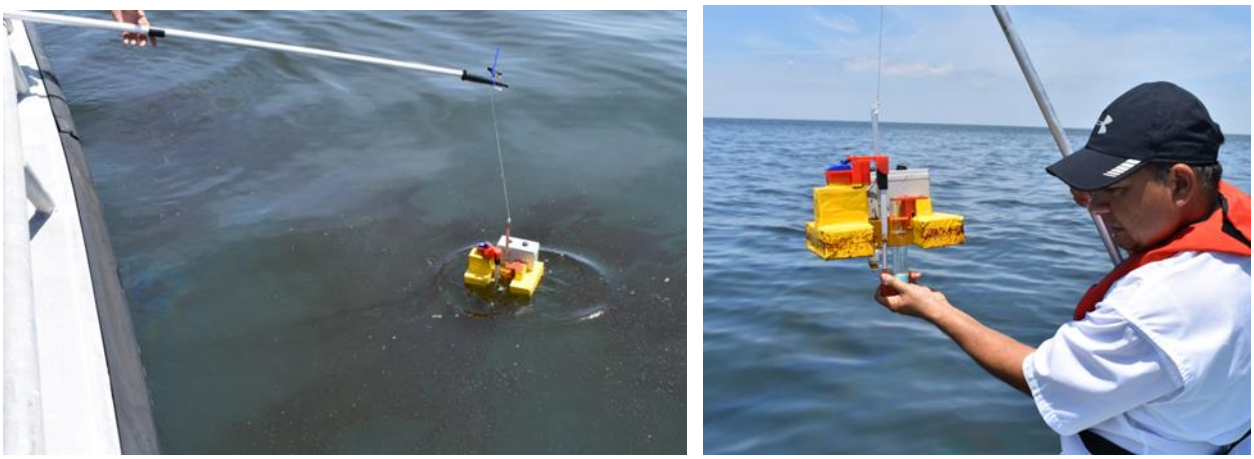

Figure 33 Collecting samples with our WM-OST for measurements of thickness

Figure 34 shows a sample collected for measuring its thickness. The oil is photographed using a 14mm macro lens with a 24-megapixel camera (A). For records, we also collect a photo from the top of the tube to show the oil from above the profile (B) which helps to visualize how close is the inner ring of the oil inside the tube. We then proceed to measure cross sections of the layer of oil to see its length in pixels units.

This sample above was collected on December 10th at 11:49 am at 29.391N and -89.788W, and its thickness measurement resulted of 90 μm. Using ultra-high-resolution photography, this thickness is obtained by measuring the length of the layer of oil inside the tube. This length is measured digitally, while obtaining the average of number of pixels for several cross sections of the layer (Figure above-C). We then proceed to use the calibration curves of the Sweet Louisiana, HOOPS, and West Texas Oil (which are very similar). The calibration curves of these three oils indicate that an average of 250 pixels of length on this layer would correspond to a thickness of 90 μm.

This procedure to measure the thicknesses of the oil slicks was repeated for all the samples obtained during the spill. We measured oil thicknesses ranging from 65 μm to 720 μm. We targeted different thicknesses across the slick so we could have a wide range of thicknesses to analyze on our UAS multispectral imagery.

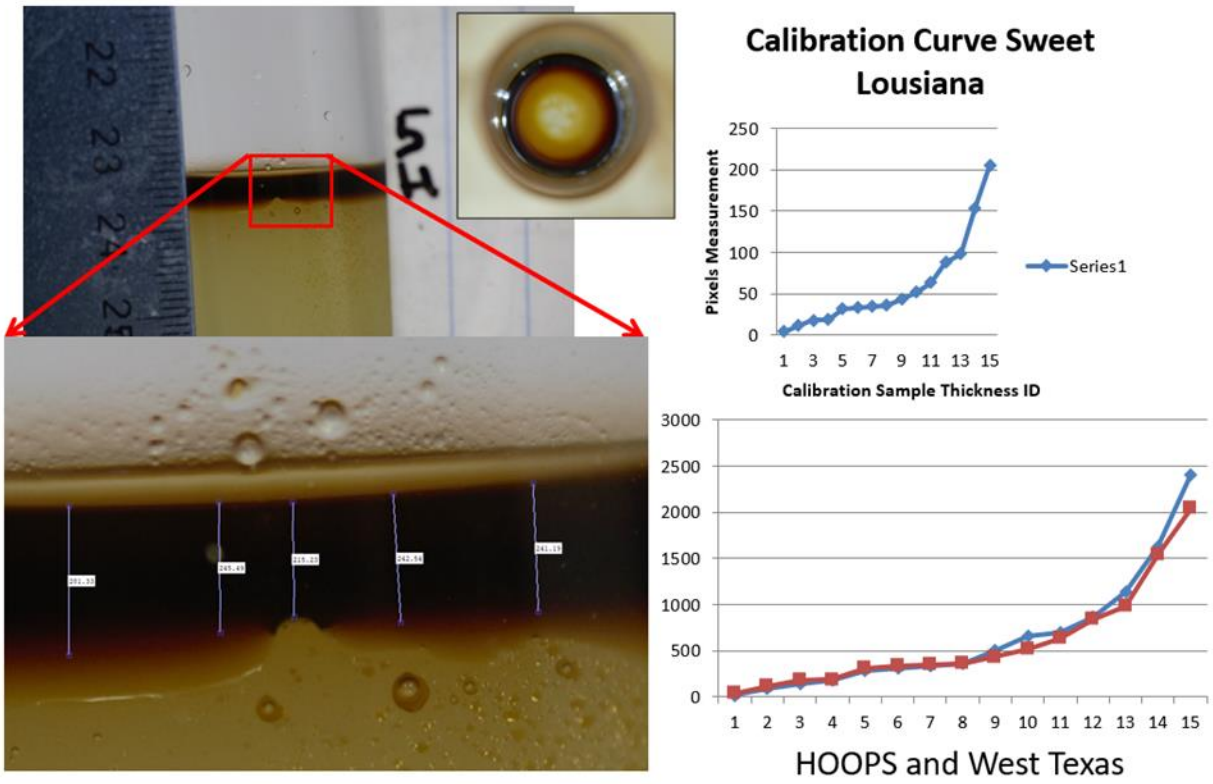

Figure 34 Sample collected for measuring its thickness

On Figure 35, the first photo (upper left) corresponds to a control sample. For visualization, samples are arranged with increasing thickness. The table on Figure 36 shows the samples as they were collected in chronological order.

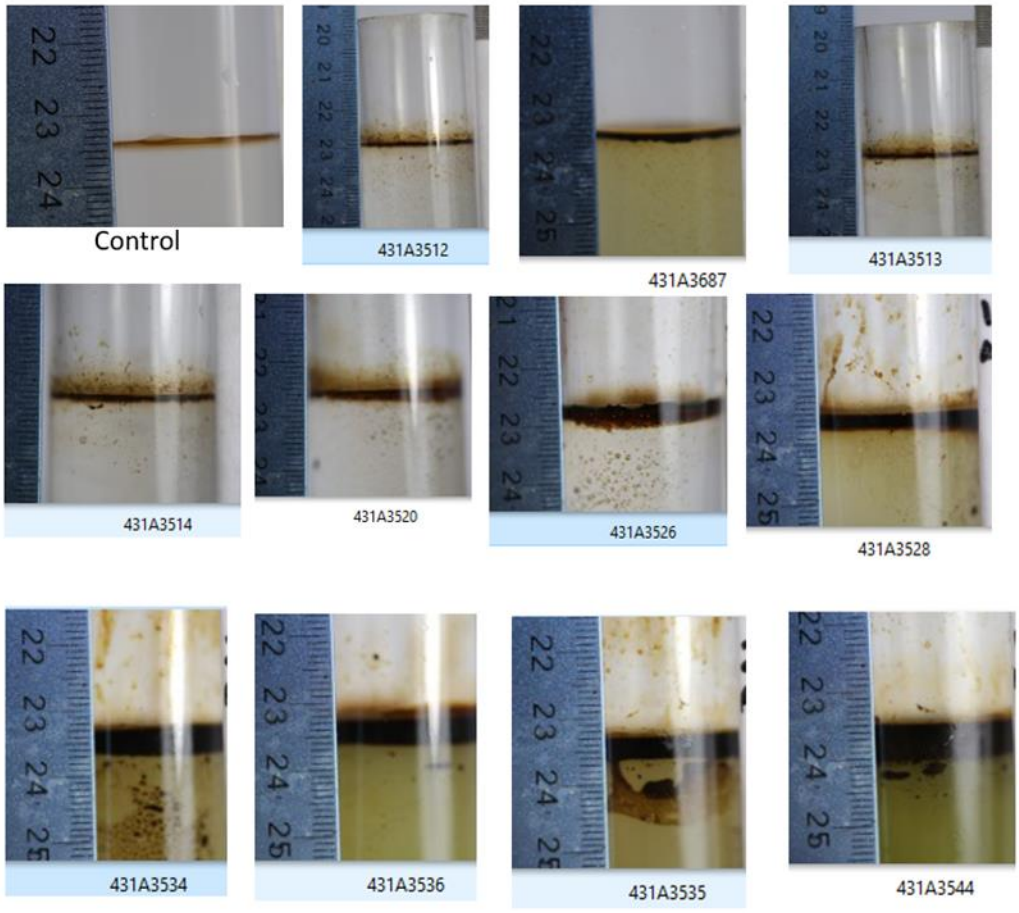

Figure 35 Samples (11) collected during the Lake Washington Spill.

Sample ID	*Longitude*	*Latitude*	*Thickness (um)*	*Description*
WM_OST_1	-89.78610	29.39536	***280***	Fresh Crude
WM_OST_2	-89.78811	29.39524	***400***	Fresh Crude
WM_OST_3	-89.78899	29.39191	***90***	Fresh Crude
WM_OST_4	-89.79010	29.38834	***320***	Slick with Material
WM_OST_5	-89.79038	29.38839	***440***	Slick with Material
WM_OST_6	-89.79112	29.38838	***110***	Fresh Crude
WM_OST_7	-89.79056	29.38869	***640***	Fresh Crude
WM_OST_8	-89.78865	29.38987	***720***	Fresh Crude
WM_OST_9	-89.79074	29.38712	***65***	Emulsion
WM_OST_10	-89.79046	29.38701	***520***	Emulsion
WM_OST_11	-89.79035	29.38629	***80***	Emulsion

Figure 36 Samples collected during the Lake Washington Spill in chronological order.

5.2 Helping the spill responders on scene with the Real-Time Oil Spill Detection System.

While we were collecting data with our multispectral UAS, some of the on-scene responders approached us in search for help. They asked us whether we could help them to see from the air the positioning of their containments (booming) as they were trying to corral the oil slick where the thickest patch of oil was moving. They came onboard our vessel (Mr. Heath Matherne from ES&H on Figure 37) and we used our real-time thermal and optical cameras to show them the extent of the oil and the location of the thickest patches. Very rapidly they coordinated their boats via radio, and we were able to navigate them (using our aerial real time view) so they could efficiently deploy their containments (Figure 38).

Figure 37 Mr. Heath Matherne from ES&H using our aerial real time view

Figure 38 Aerial view of the containments (booming)

The aerial view shown in Figure 39 shows the vessel deploying the boom on an area where the currents are taken the thickest patch of oil downstream. The white boom is secure by poles that are stacked in the sea floor.

Figure 39 shows the moment in which the containment is being deployed, intersecting the thickest patch of oil. Figure 40 shows when the containment after being fully installed. The oil spill responders where able to efficiently cover the main stream of thick oil containing the

highest amount of oil possible. Our real time aerial view was very useful for them to achieve this result in a timely manner.

Figure 39 Vessel deploying the boom

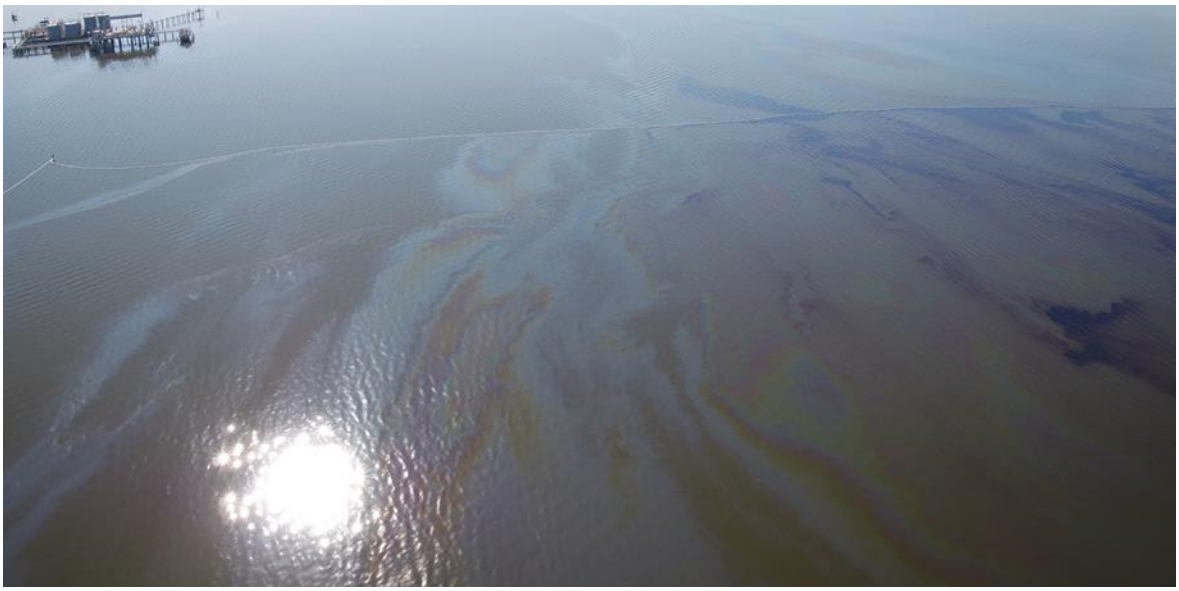

Figure 40 Containment fully installed

6. UAS Multispectral imagery

After imagery is collected by the multispectral sensors, we proceed to download the imagery from all the cameras from the UAS to our laptop. All the UAS images are then passed through a routine that generates the projection of each independent channel. This routine assigns a spatial extent for each channel layer by creating a 'worldfile' for each of the image files. The routine was developed in Matlab and it also creates a directory structure where each image is saved as '.jpg' format and the geospatial extent is saved as a worldfile. This configuration makes easier the job of inspecting the imagery in a GIS platform. The example shown in Figure 41 displays how individual spectral channels are projected. This shows 4 of the main multispectral bands that are used for the determination of thickness. If one compares the multiple channels there can be seen differences on how the oil is imaged at different wavelengths.

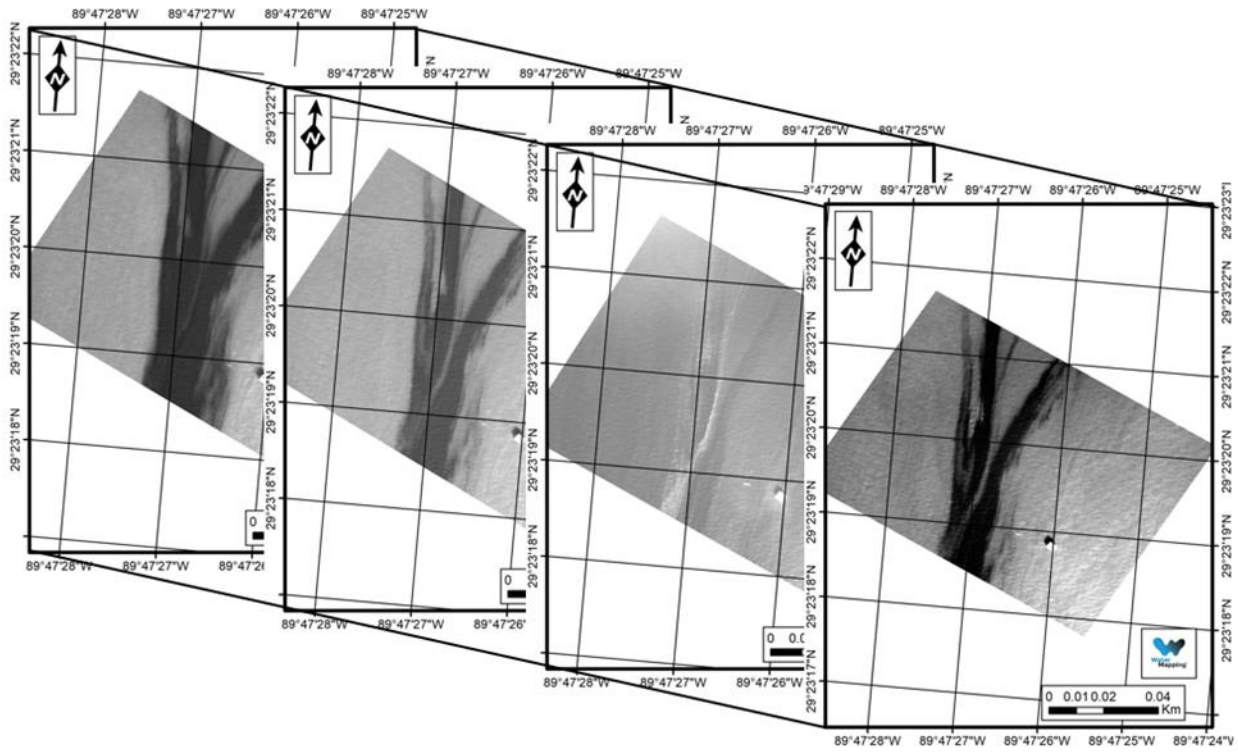

Figure 41. Projection of independent UAS multispectral channels.

The projection routine reads the GPS information embedded on each multispectral image as well as the flight logs on the UAS. By matching the time of the image with the flight log we can link the GPS information with the heading of the UAS (and therefore with the orientation of the camera). This information provides the parameters for height, heading, and scale needed to generate the projection of each individual frame.

6.1 Multispectral calibrated reflectance

By combining the R-G-B channels of the multispectral UAS imagery, we can generate a calibrated true color of the sea surface. This procedure helps to see a clear improvement between the non-calibrated reflectances versus the calibrated bands. On Figure 42 is shown a calibrated still where a thick patch of oil is shown on the center. Towards the sides of the thick oil there can be seen several levels of rainbow sheens. By looking at this RGB combination it would be hard to make a further distinction of thickness, therefore this could only be useful to classify between heavy thick oil and sheens.

Despite the limitation on the thickness classification this view is useful to get a sense of the true extent of the oil. Just like at Ohmsett, visual range of vision (RGB) is good to realize a sense of the scale of the features. For example, the scale on this map shows that the cross section of the thick patch of oil is approximately 20m. (at the middle). This RGB composite is generated with the maximum resolution available which would be of approximately 0.5 cm resolution achieved by flying at 400ft.

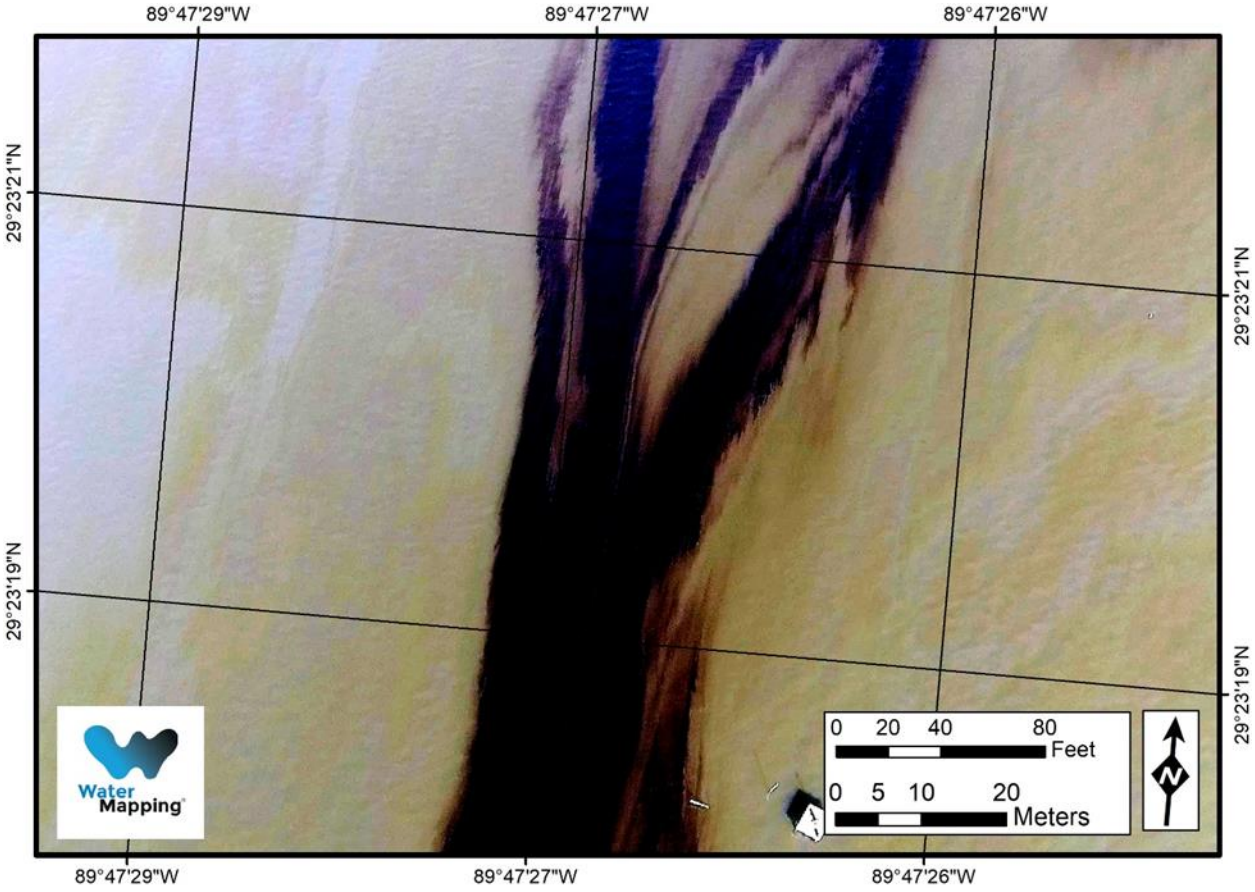

Figure 42 Calibrated RGB (True color) reflectance of the oil slick.
This aerial view is generated by combining the Red, Green, and Blue channels from the multispectral bands of the UAS.

6.2 Thermal

The multispectral UAS includes channels on the long wave infrared that we use to get calibrated thermal imaging. Figure 43 shows an overlay of the thermal image on top of the calibrated reflectance RGB. The thermal signature on this thick patch of oil has a heterogenous variance throughout the thick portion of the slick which is directly related to the thickness of oil.

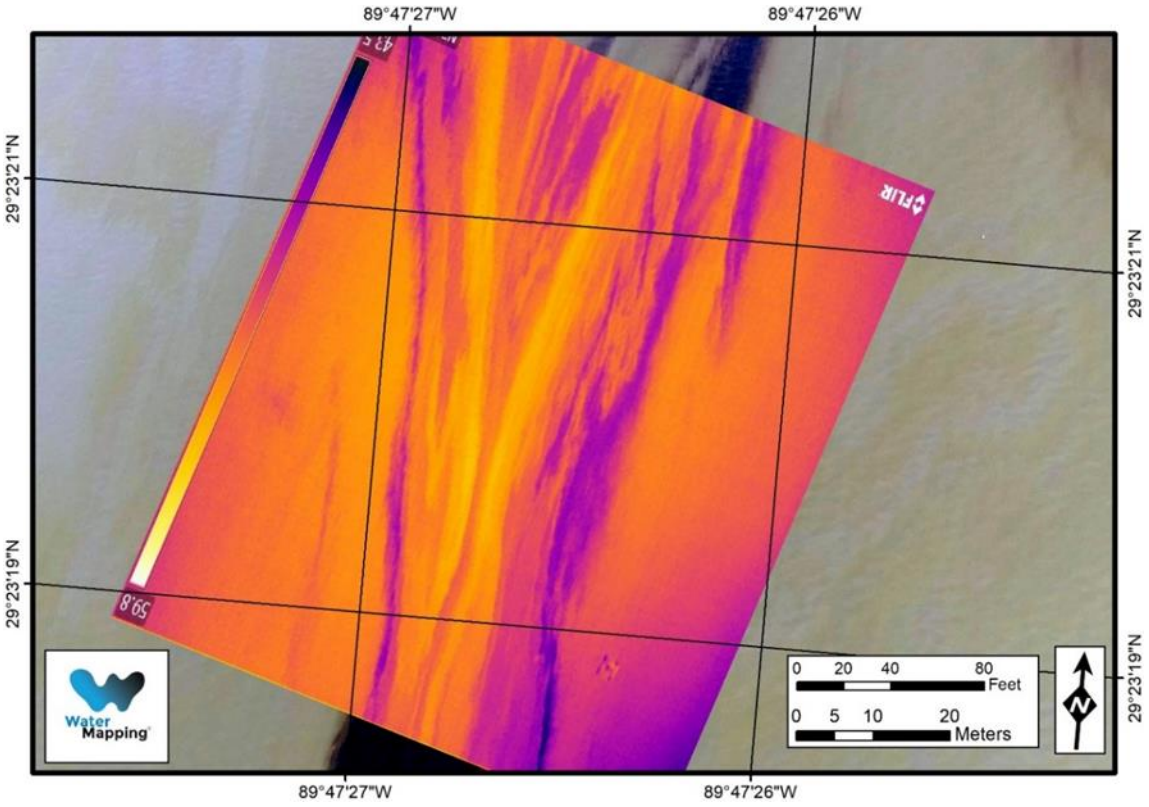

Figure 43. Thermal imaging of the thick oil.
The orientation of the map is toward the north (up) and the flight direction was towards the south, which is why the thermal scale and the 'FLIR' symbols shows up upside down.

A closer look of the thermal imaging reveals the variances on the temperature levels. For example, the interface of the software shown on Figure 44 shows the temperature change inside the box in the middle of the screen. The warmest area inside the box was 56.1 °F while the coolest was 47.1 °F. The maximum difference of 9 degrees Fahrenheit is huge and indicates a large range of thicknesses suggesting that the thickest (warmest) could be on the rage of actionable oil.

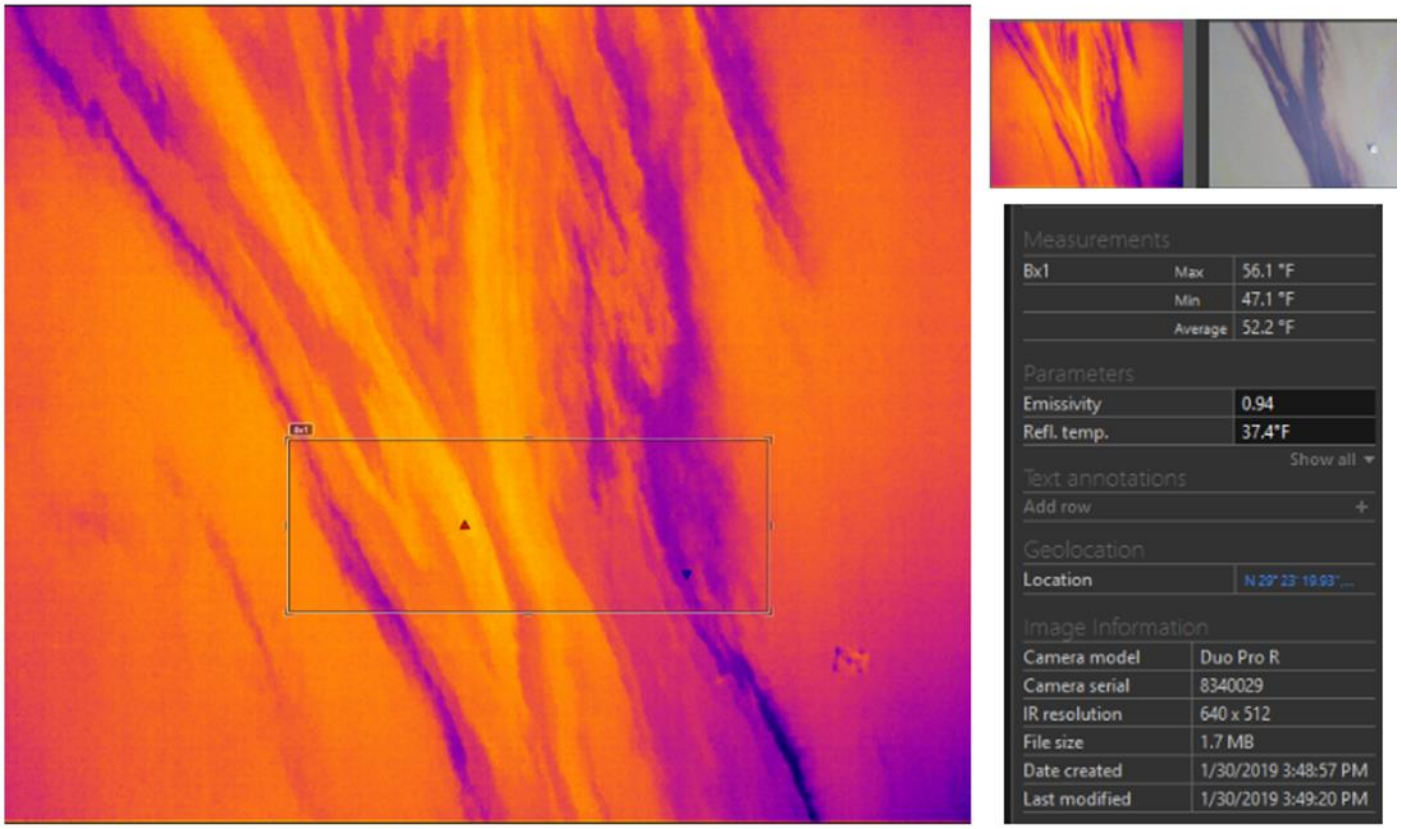

Figure 44. Thermal imaging of the thick oil with calibrated temperature readings.
Our algorithm retrieves the temperature of each pixel and relates that temperature with the multispectral UAS data.

6.3 Rainbow sheens detected on 475nm channel

The thermal data itself reveals many levels of thicknesses that can be used to determine different classes of thickness of the oil slick. When there is a layer of thin oil (on the Rainbow sheen level) one should not expect a big thermal contrast between the surface water and the oil sheen. In other words, it is harder to detect the oil on the thermal imaging unless it is thick enough to create a

thermal variance. This is the reason we use the channel with the 475nm from the multispectral data (Figure 45). If we look at the 475nm channel (which is in the visual range), we can observe that towards the sides of the heaviest thickest oil (black patch on the middle) there are variances that correspond to the rainbow sheens.

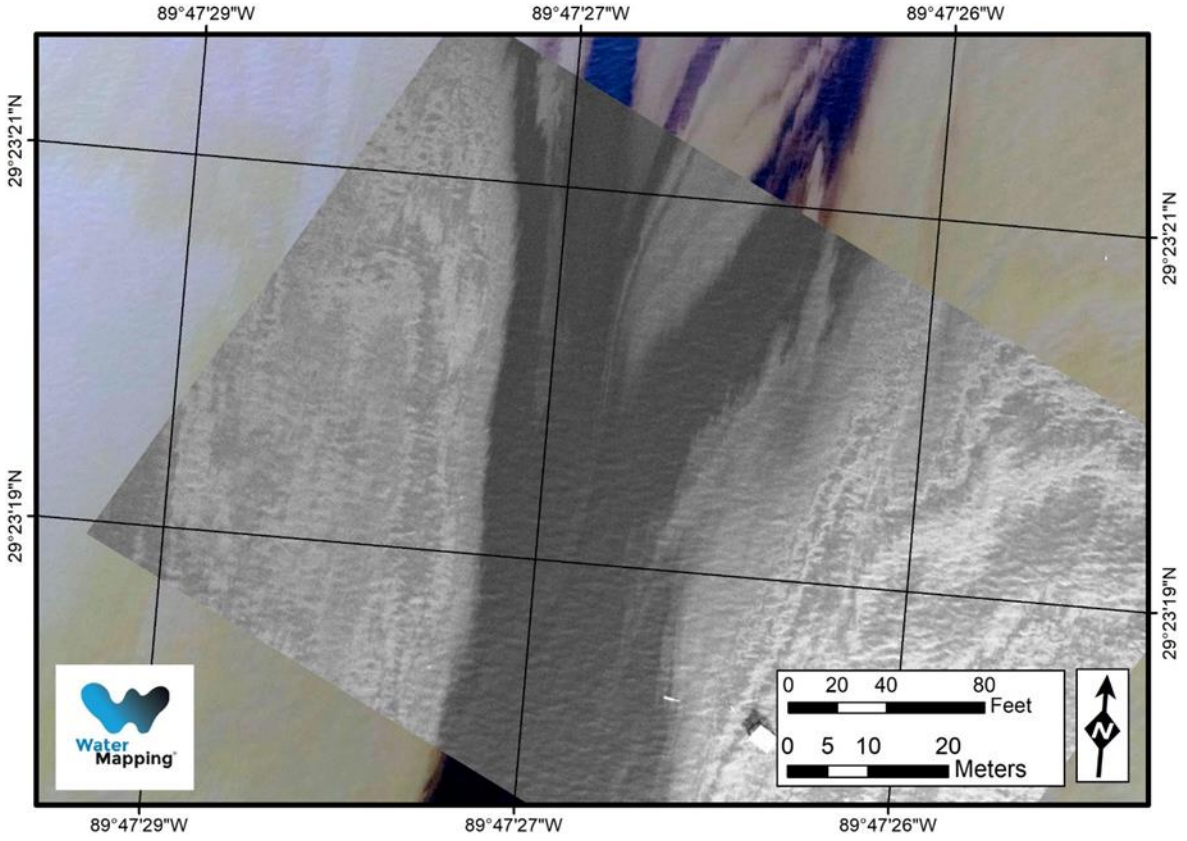

Figure 45. The 475nm channel.
This channel is used to detect rainbow sheens around the thickest patch of oil.

The variances of tones on this panchromatic image represents the presence of sheens and rainbow-sheens that fall on the category of thin oils of up to 5 μm in thickness. These are not considered actionable but are important to discern because this channel would help to distinguish false positives like sargassum or any suspended materials other than oil.

6.4 Oil Thickness classifications.

With the ability to combine the thermal and the multispectral data we can create thickness classification products. For example, Figure 46 is a classification that can be created near real time for oil spill responders. In Figure 46, the "Thick" class would correspond to oil above 100 µm, the "Thickest" class would correspond to oil above 200 µm, while the Thin would be equivalent to oil of up to 50 µm in thickness.

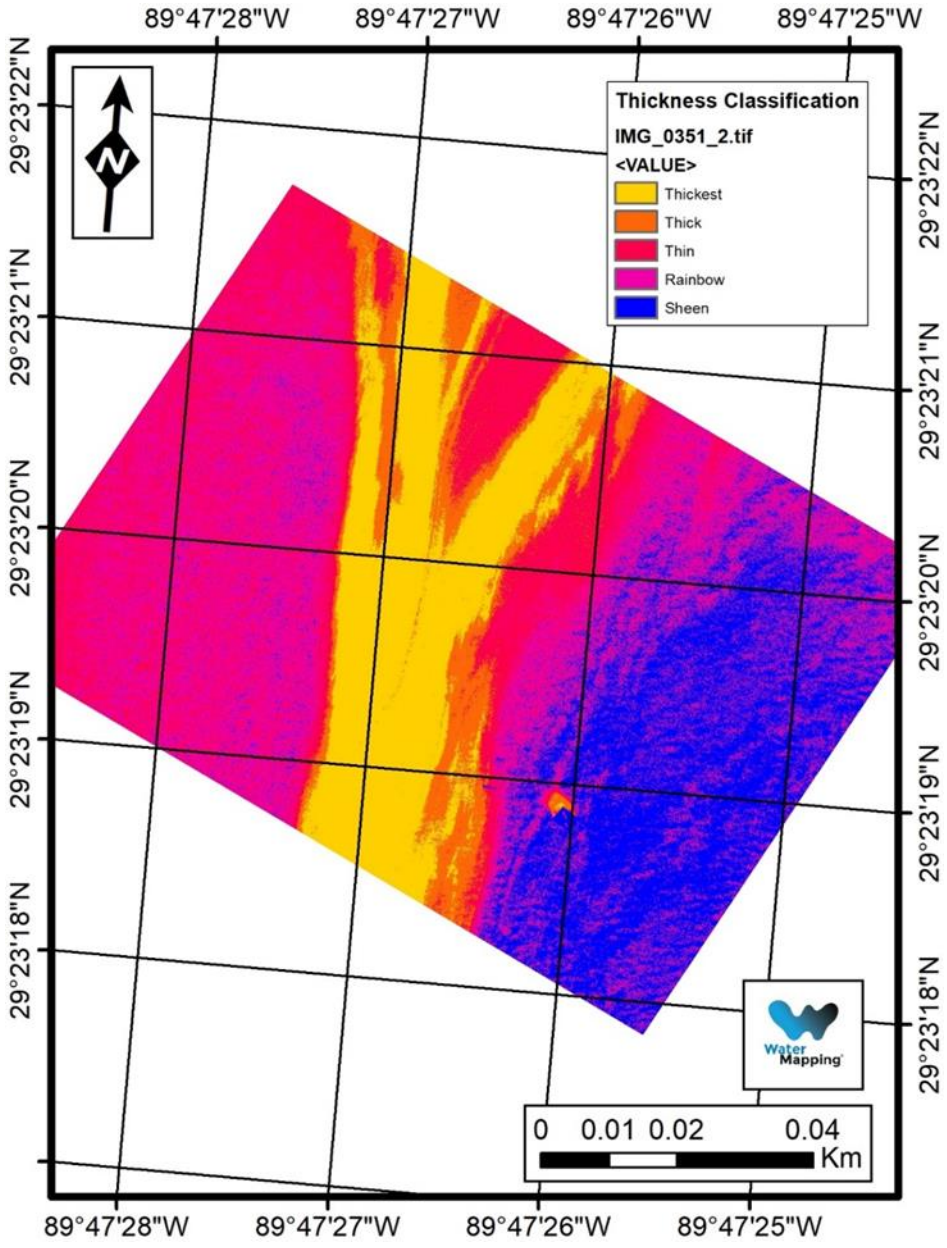

Figure 46. Oil thickness classification.
Based on qualitative classification of Actionable (Thickest and Thick) and non actionable (Thin-Rainbow-Sheen)

Another way to classify the thicknesses would be based on the level of emulsification. Figure 47 uses the near infrared channel to identify the portion of the floating oil that has the highest content of water on the emulsion (red color) vs the fresher oil (yellow or transparent color)

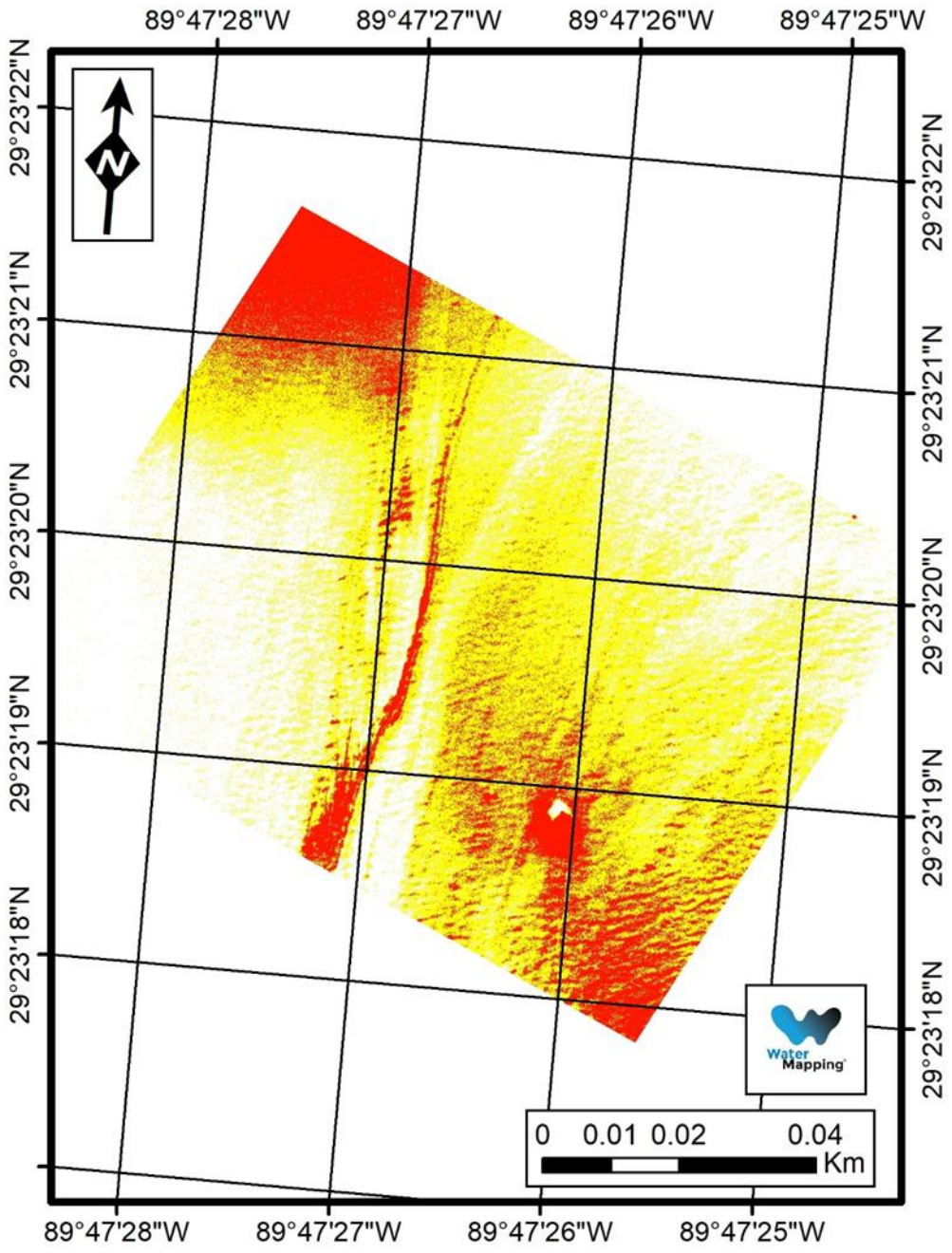

Figure 47. Classification for discerning emulsified oil (red) from fresh crude (yellow).

The red classification shown on Figure 48 would correspond to fresh oil with no water content which could be treated by a controlled burn. However, the two classes together shown on Figure 49 (red and blue) should be considered as recoverable with either booms or skimmers.

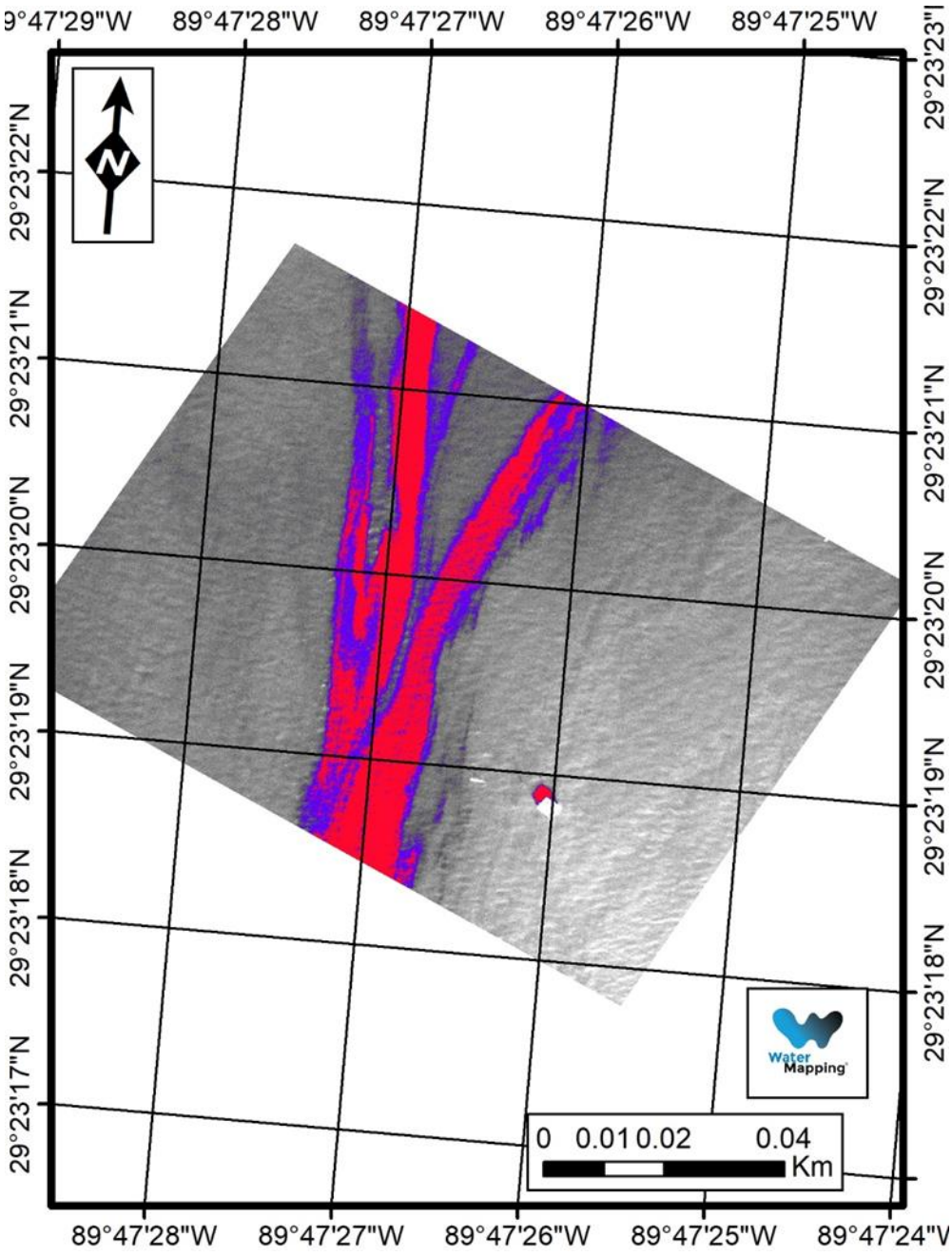

Figure 48. Actionable oil for burning (red) or recovery (red + blue).

6.5 Creation of Orthomosaics

The individual UAS multispectral images can be combined to create orthomosaics (Figure 49). These orthomosaics are created as a single layer (one per channel) and then combined to create thickness classifications. Examples below are orthomosaics of 6 different bands with an approximate length of 1km. The channels are A) 475nm, B) 560nm, C) 669nm, D) 717nm, E) 880nm, F) 940nm

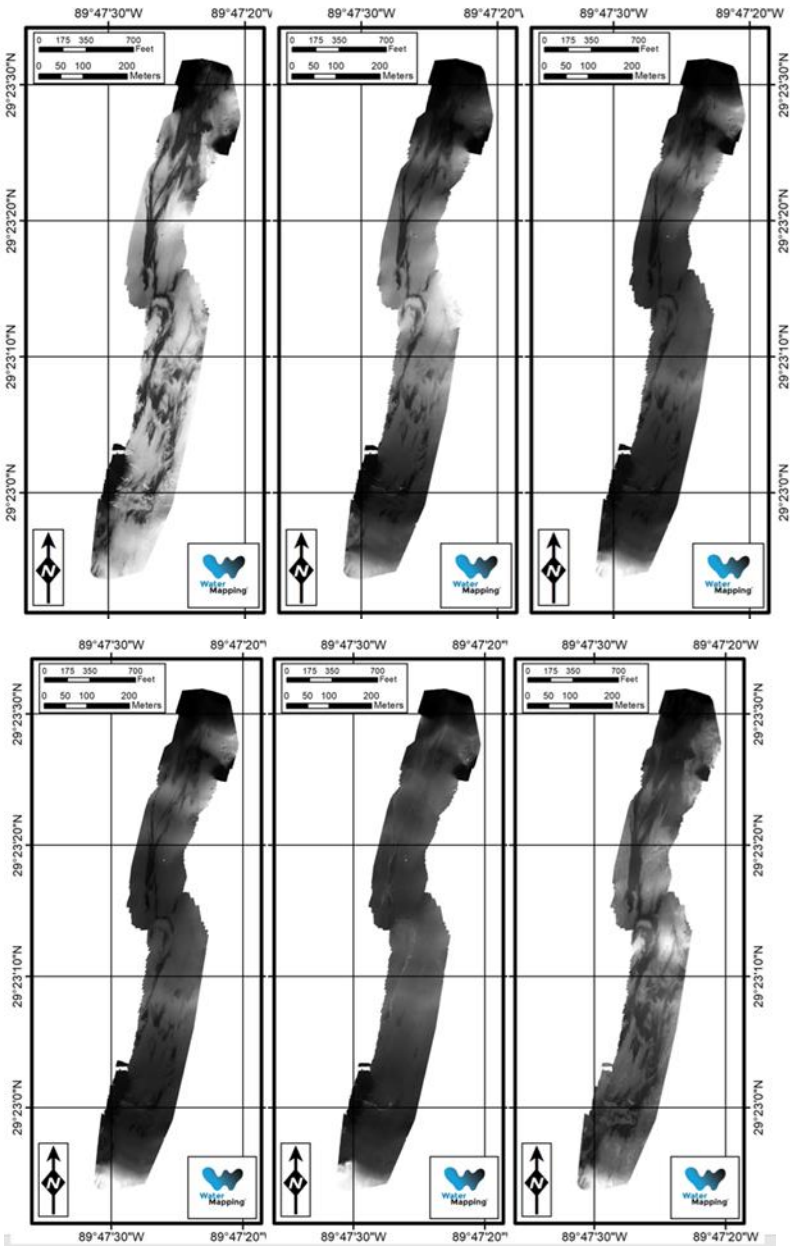

Figure 49. Orthomosaics of independent channels.

6.6 Orthomosaic classification.

Using the individual orthomosaics we can use the same combinations shown from Figures 46 to 48 to create classifications of oil based on thicknesses. For example, Figure 50 would correspond to a classification of Actionable and non-actionable oil.

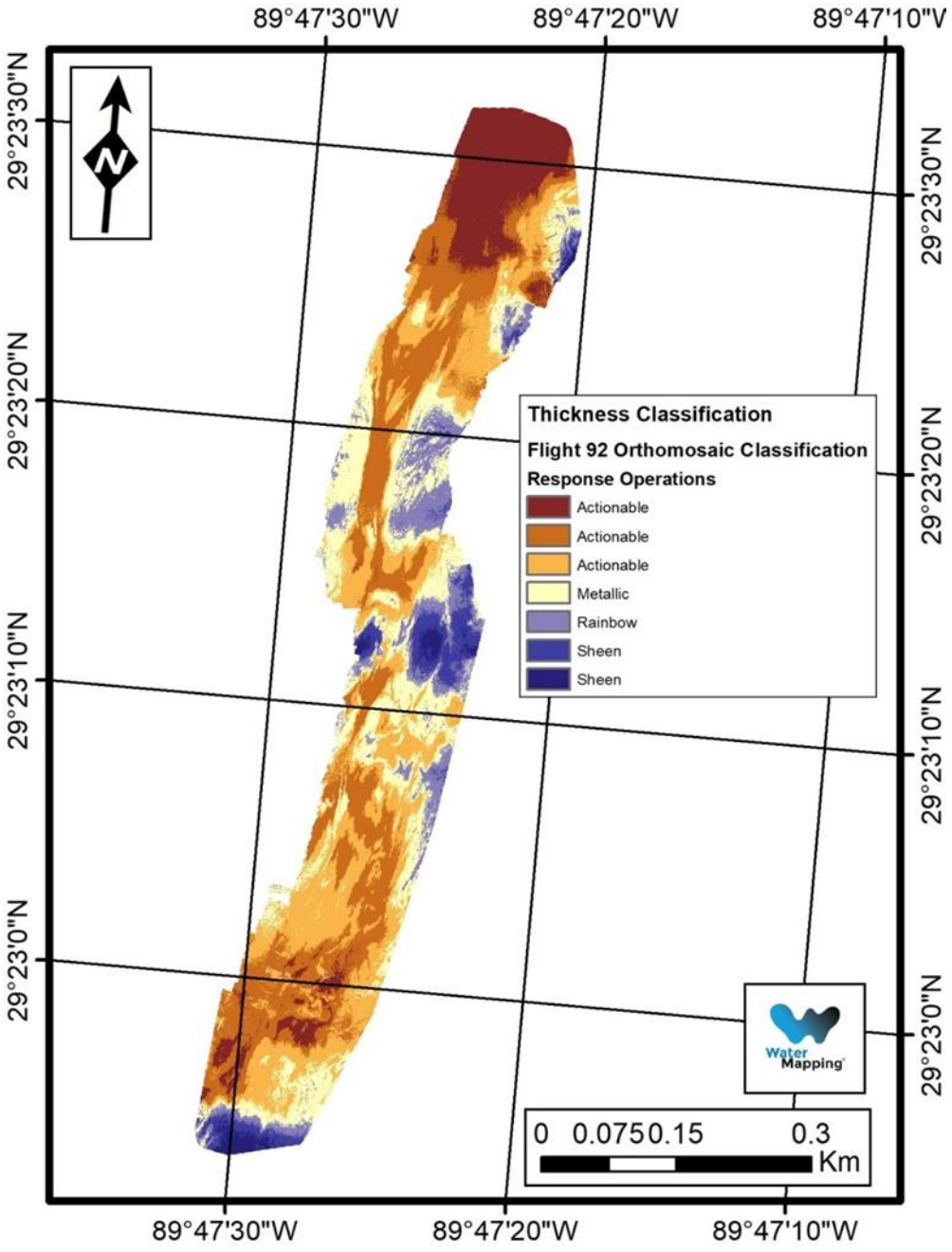

Figure 50. Orthomosaic classification of actionable and non-actionable oil.

It is important to point out that during the spill a Worldview-2 image was acquired. This satellite image was collected at 11:45 am CT, and the UAS data was collected approximately 23 minutes later at 12:08pm CT.

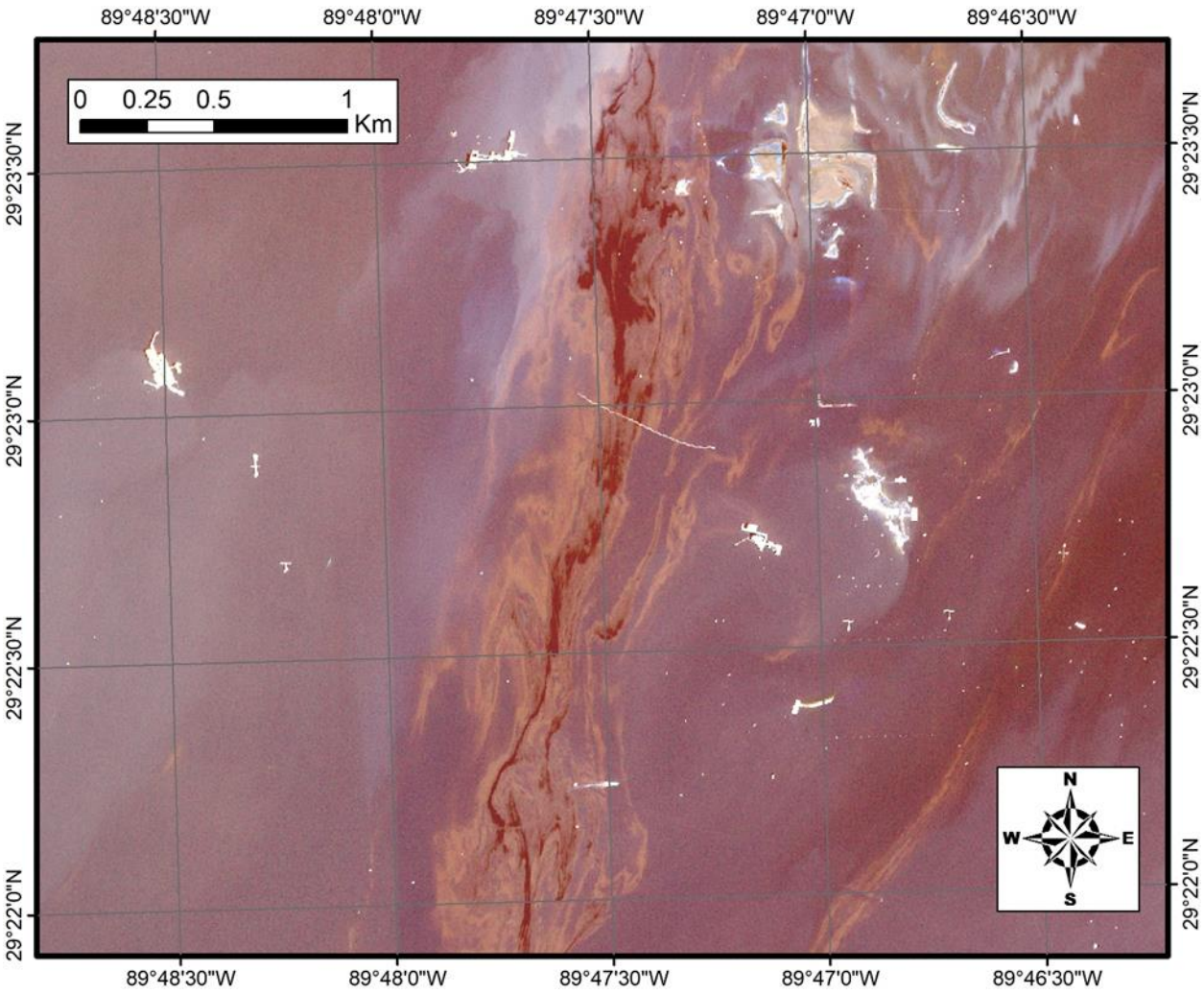

Figure 51 WorldView-2 image captured during the spill

The WorldView-2 image validates the data collected by our UAS. Worldview-2 is multispectral satellite image with 5 bands matching our multispectral UAS data. What that means is that, with the incorporation of our thickness measurements and our spatial UAS classifications, we can attempt to generate a similar classification using the multispectral satellite bands.

Using the thicknesses measured with WM-OST we can assign thickness values to the classes obtained on the previous map shown on Figure 50. This classification is then overlay on the satellite image Worldview-2 obtained during the spill as shown of Figure 52.

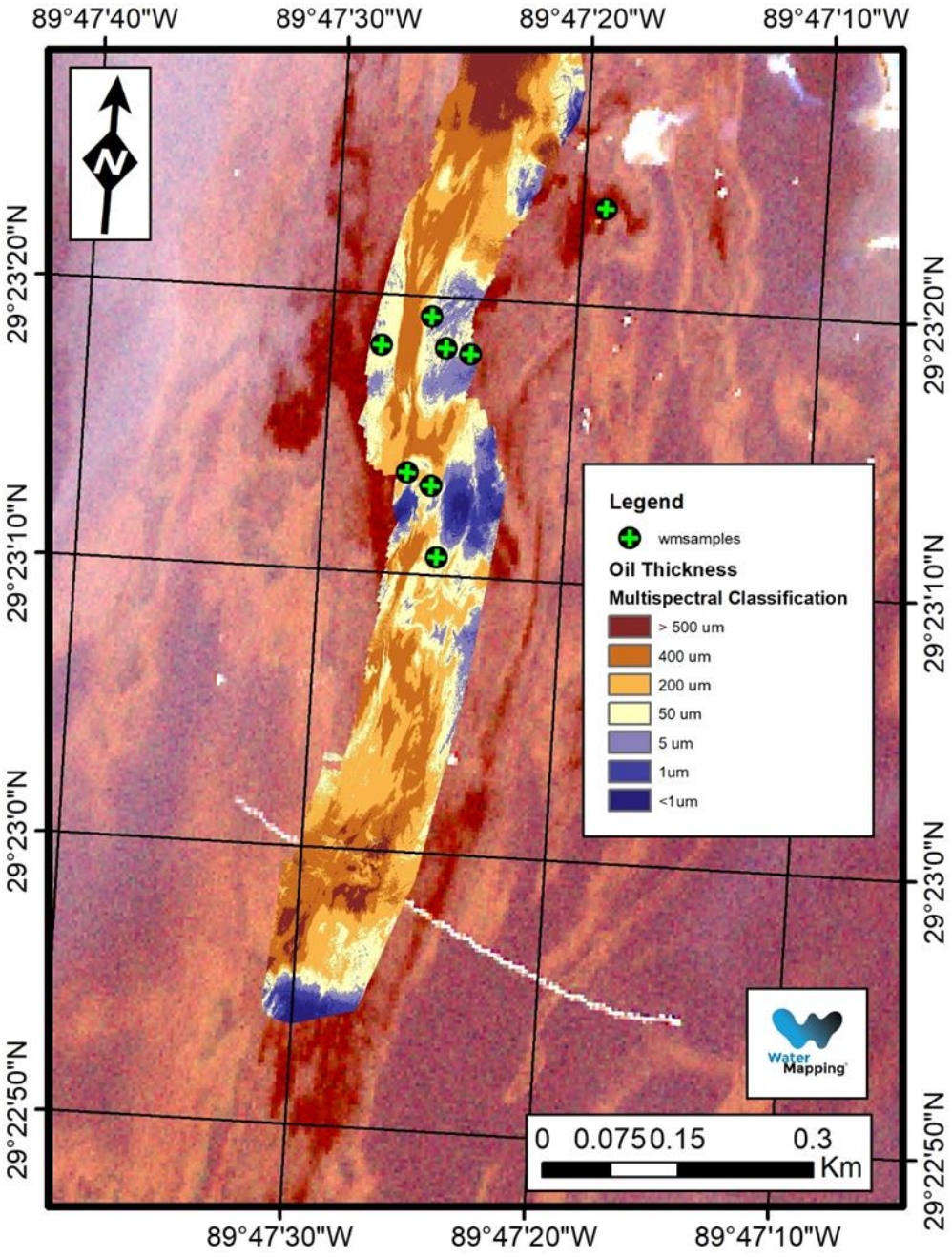

Figure 52 Incorporation of thickness measurements on the UAS classifications and overlay on the Worldview-2 image.

Figure 53 would be a two-class satellite product of the oil spill. This is an example of how we could extrapolate the UAS and WM-OST samples for the entire slick

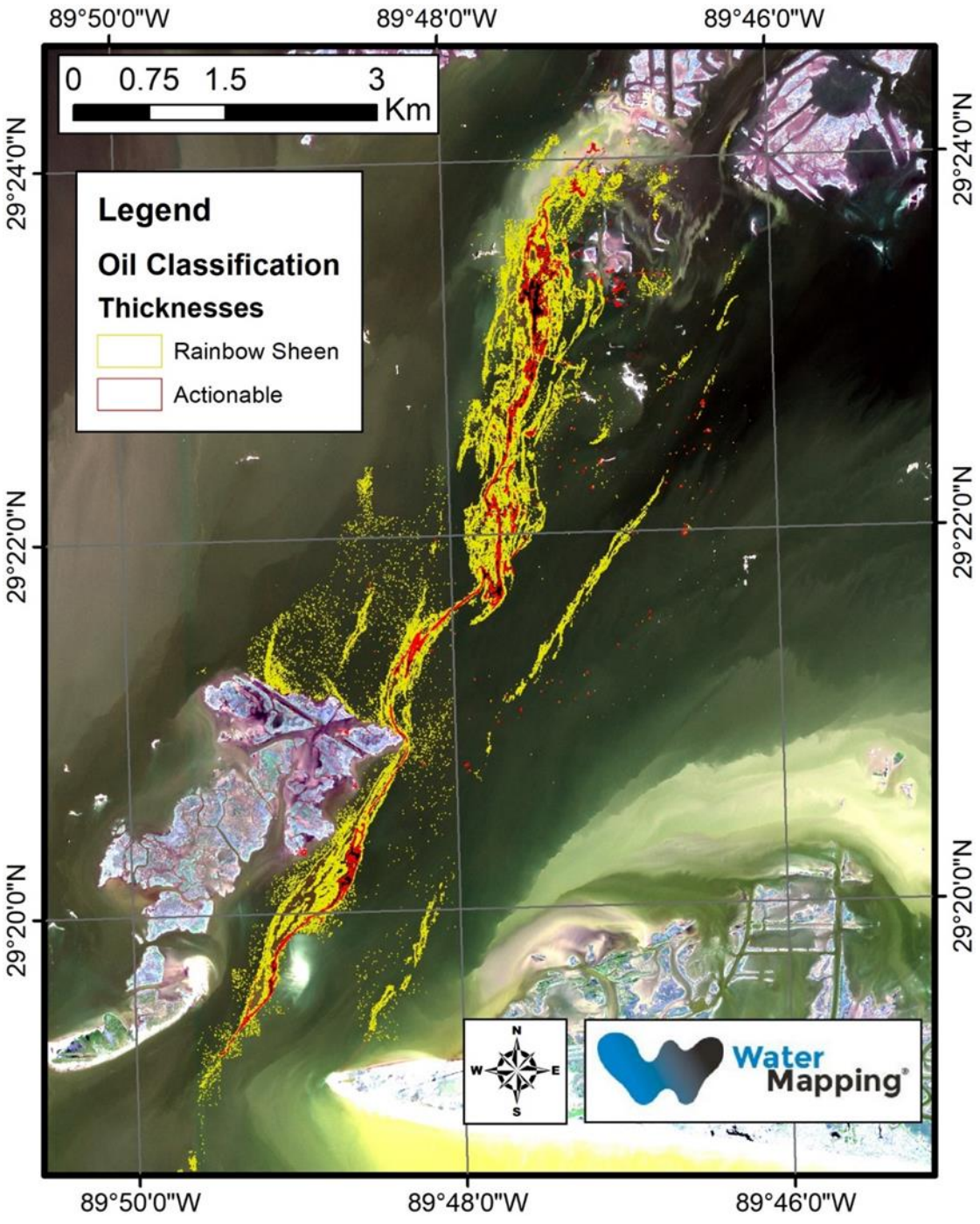

Figure 53 Two-class satellite product of the oil spill and overlay on the Worldview-2 image

7. Discussion

7.1. What has been achieved?

This report implemented a combination of literature reviews, laboratory experiments, and field testing along with carefully designed equipment, highly specialized techniques and unique experimental settings. Several significant findings have been achieved in this project, among which are:

1) Oil is very heterogenous and patchy, regardless of oil type (crude oil or oil emulsion) or the size of the water tank. Even under calm conditions, the patches can range from a few millimeters to decameters in size. This finding has significant implications on both measurements and data interpretation. It is difficult to associate a single hyperspectral measurement of a finite footprint with the patchy oil, but imaging cameras should be used to measure the spectra of each individual pixel. This is why imaging cameras were used in this study. For data interpretation, reflectance spectra from coarse-resolution satellite image pixels correspond a mixture of different oil patches with possibly oil-free water. Therefore, interpretation of such coarse-resolution pixels must to consider the mixture of different oil thickness.
2) The two experiments (USF oil tank experiment and Ohmsett experiment) resolve the puzzle of the inconsistent results from the literature. Oil-water spectral contrasts can be very different between crude oil and emulsified oil. The former has most of the spectral response in the blue-green wavelengths while the latter has most of the spectral response in the NIR-SWIR wavelengths. For each oil type, the responsive wavelengths have definitive relationships with oil thickness.
3) For oil emulsions, the most responsive wavelengths are in the SWIR region. Therefore, whenever possible, these wavelengths should be used to classify oil type and estimate oil thickness. When these wavelengths are not available, they may be substituted by NIR wavelengths.
4) Although hyperspectral data can show definitive oil signatures in the SWIR wavelengths due to the C-H bond absorption, most remote sensing platforms are not equipped with hyperspectral sensors. In this case, multi-band sensors can be used as alternatives if the bands are carefully selected. In this project, these bands were selected to be 475 nm, 560 nm, 668 nm, 717 nm, and 840 nm, with additional bands at 880 nm and 940 nm when possible. The two experiments show that such band settings on the imaging cameras are effective in classifying oil types and estimate oil thickness.

5) Thick oil, either in crude form or in emulsified form can be detected and distinguished by thermal cameras in an adequate manner.
6) For multi-band images, a three-step approach can be developed to classify oil types (crude oil and oil emulsions) and estimate oil thickness in each type. The approach is developed here, which shows its effectiveness when applied to multi-band data resampled from AVIRIS measurements.
7) Finally, the use of a black tarp in the Ohmsett experiment is a necessary step to simulate a realistic marine environment, as the bright water background (due to bottom reflection) makes it unrealistically easy to differentiate oil from water.

7.2 Uncertainties, gaps, and future works

Commercially available imaging cameras, when mounted on UAS platforms, may provide unique values of providing multi-band spectral reflectance of each individual pixel as long as the cameras are calibrated through the procedures presented here. However, the calibration is not trivial. In addition, some inherent camera artifacts need to be treated carefully, such as striping noise, stray light, and vignette effect. Further efforts are required to develop methods to correct these artifacts automatically.

Lastly, due to technical difficulties, the most valuable band in the SWIR wavelengths could not be used on any of the imaging cameras. However, the SWIR wavelengths are better than NIR wavelengths in their responses to oil emulsions and changing thicknesses. In future works, whenever feasible, SWIR bands may be added to the imaging cameras to improve the measurements and interpretations.

Conclusion

The multispectral cameras were successfully tested on the UAS during Ohmsett near real time demonstration and during the Lake Washington Spill. The datasets collected during the Lake Washington spill can be further explore to develop classification algorithms for coastal mapping and detection of oil in the shoreline. Despite numerous published studies on the implementation of remote sensing to assess oil spills, oil spill remote sensing still faces significant challenges in both technology development and algorithm design. This is partly due to lack of understanding of oil-water spectral and spatial contrasts in the real environments. Through carefully selected instrumentation and carefully designed oil tank and Ohmsett experiments, oil-water spectral and spatial contrasts are better understood, from which a 3-step approach is developed to classify oil type (crude oil versus oil emulsion) and to estimate oil thickness.

References

Byfield, V. (1998). Optical remote sensing of oil in the marine environment. In: University of Southampton

Clark, R.N., Swayze, G.A., Leifer, I., Livo, K.E., Kokaly, R., Hoefen, T., Lundeen, S., Eastwood, M., Green, R.O., & Pearson, N. (2010). A method for quantitative mapping of thick oil spills using imaging spectroscopy. US Geological Survey Open-File Report, 1167, 1-51

Hu, C., L. Feng, R. F. Hardy, and E. J. Hochberg (2015). Spectral and spatial requirements of remote measurements of pelagic Sargassum macro algae. Remote Sensing of Environment, 167, 229-246, doi:10.1016/j.rse.2015.05.022.

Lammoglia, T., & Filho, C.R.d.S. (2011). Spectroscopic characterization of oils yielded from Brazilian offshore basins: Potential applications of remote sensing. Remote Sensing of Environment, 115, 2525-2535

Lu, Y., Tian, Q., Wang, X., Zheng, G., and Li, X. (2013), Determining oil slick thickness using hyperspectral remote sensing in the Bohai Sea of China, International Journal of Digital Earth, 6, 76-93

Lu, Y., W. Zhan, and C. Hu (2016). Detecting and quantifying oil slick thickness by thermal remote sensing: A ground-base experiment. Remote Sensing of Environment, 181, 207-217, doi:10.1016/j.rse.2016.04.007.

Lu, Y., W. Zhan, and C. Hu (2016). Detecting and quantifying oil slick thickness by thermal remote sensing: A ground-base experiment. Remote Sensing of Environment, 181, 207-217, doi:10.1016/j.rse.2016.04.007.

Otremba, Z. and J. Piskozub (2001). Modelling of the optical contrast of an oil film on a sea surface. Optics Express, 9(8), 411-416

Otremba, Z. and J. Piskozub (2003). Modeling the remotely sensed optical contrast caused by oil suspended in the sea water column. Optics Express, 11(1), 2-6

Otremba, Z., O. Zielinski, and C. Hu (2013). Optical contrast of oil dispersed in seawater under windy conditions. Journal of the European Optical Society - Rapid publications, 8, p. 13051

Sun, S., Hu, C., Feng, L., Swayze, A.S., Holmes, J., Graettinger, G., MacDonald, I., Garcia, O., & Leifer, I. (2016). Oil slick morphology derived from AVIRIS measurements of the Deepwater Horizon oil spill: Implications for spatial resolution requirements of remote sensors. Marine Pollution Bulletin, 103, 276-285

Svejkovsky, J. and J. Muskat (2006), Real-time Detection of Oil Slick Thickness Patterns with a Portable Multispectral Sensor, in Final Report submitted to the U.S. Department of the Interior, Mineral Management Service, 31 July 2006. p. 77

Svejkovsky, J., Lehr, W., Muskat, J., Graettinger, G., & Mullin, J. (2012). Operational utilization of aerial multispectral remote sensing during oil spill response. Photogrammetric Engineering & Remote Sensing, 78, 1089-1102

Wettle, M., Daniel, P.J., Logan, G.A., & Thankappan, M. (2009). Assessing the effect of hydrocarbon oil type and thickness on a remote sensing signal: A sensitivity study based on the optical properties of two different oil types and the HYMAP and Quickbird sensors. Remote Sensing of Environment, 113, 2000-2010

Department of the Interior (DOI)

The Department of the Interior protects and manages the Nation's natural resources and cultural heritage; provides scientific and other information about those resources; and honors the Nation’s trust responsibilities or special commitments to American Indians, Alaska Natives, and affiliated island communities.

Bureau of Safety and Environmental Enforcement (BSEE)

The mission of the Bureau of Safety and Environmental Enforcement (BSEE) works to promote safety, protect the environment, and conserve resources offshore through vigorous regulatory oversight and enforcement.

BSEE Response Research Branch Program

The Response Research Branch (RRB) oversees the Oil Spill Response Research Program (OSRR) and manages the National Oil Spill Response and Renewable Energy Test Facility (Ohmsett). The research conducted under OSRR aims to improve oil spill response and preparedness by advancing the state of science and the technology used in responding to offshore oil spills. The research also supports the Bureau’s needs while ensuring the highest level of scientific integrity by adhering to BSEE’s peer review protocols. The proposal, selection, research, review, collaboration, production, and dissemination of each of BSEE’s Response Research Branch Program follows the DOI Code of Scientific and Scholarly Conduct, in support of a culture of scientific and professional integrity, as set out in the DOI Departmental Manual (305 DM 3).